



CONSTRUCTION AND CONTROL OF AN AERIAL VEHICLE FOR CROP MONITORING



MASTER IN OPTOMECHATRONICS

Advisor:

PhD. Gerardo Ramón Flores Colunga

Student:

Andrés Montes de Oca Rebolledo

July 2018

León, Guanajuato, México

Contents

| | |
|---|-----------|
| Acknowledgements | 9 |
| Publications | 10 |
| Abstract | 11 |
| Introduction | 14 |
| 1 Literature review | 15 |
| 1.1 Commercial multispectral imaging systems | 15 |
| 1.2 Aerial imaging system implementation and applications | 16 |
| 2 Theoretical knowledge | 28 |
| 2.1 Introduction | 28 |
| 2.2 Quad-rotor Model | 29 |
| 2.2.1 Airspeed and groundspeed | 30 |
| 2.2.2 Euler equations | 30 |
| 2.2.3 Newton equations | 33 |
| 2.3 Multispectral properties of vegetation | 37 |

| | | |
|----------|--|-----------|
| 2.3.1 | Optical aspect of photosynthesis and its relationship with vegetation stress | 37 |
| 2.3.2 | Vegetation curve and spectral bands of vegetation | 41 |
| 2.3.3 | Vegetation indices | 44 |
| 2.3.4 | Normalized Difference Vegetation Index | 45 |
| 3 | Methodology | 47 |
| 3.1 | System description | 48 |
| 3.1.1 | Hardware components | 49 |
| 3.1.2 | Software components | 50 |
| 3.2 | Multispectral camera design | 52 |
| 3.3 | Flight trajectory | 54 |
| 3.3.1 | Photogrammetric Parameters | 55 |
| 3.3.2 | Camera Trigger System | 57 |
| 3.4 | Image post-processing | 58 |
| 3.4.1 | Georeferencing | 58 |
| 3.4.2 | Orthomosaic generation | 59 |
| 3.4.3 | NDVI computation | 59 |
| 4 | Experiments | 61 |
| 4.1 | Camera testing | 61 |
| 4.2 | Photogrammetric parameters and flight plan | 65 |
| 4.3 | Image post-processing | 69 |
| 4.3.1 | Image rectification | 69 |
| 4.3.2 | Image Georeferencing | 72 |
| 4.3.3 | Orthomosaic | 73 |
| 4.3.4 | NDVI computation | 73 |
| 4.4 | Additional experiments | 74 |
| 5 | Conclusions | 78 |

List of Figures

| | | |
|------|---|----|
| 1 | The unmanned aerial vehicle used in this work. This drone is equipped with the proposed multispectral imagery system. | 13 |
| 1.1 | Commercial multispectral imaging systems. | 16 |
| 1.2 | Spectrometer-based hyperspectral sensor. | 17 |
| 1.3 | Imaging system with external filters. | 19 |
| 1.4 | Implementation of a multispectral imaging system for NDVI computation. | 20 |
| 1.5 | Multispectral imaging system implemented in a rotary-wing vehicle. | 21 |
| 1.6 | Hyperspectral imaging system implemented on a octa-rotor. | 21 |
| 1.7 | Imaging system implemented in a fixed-wing UAV platform. | 22 |
| 1.8 | NDVI obtained with a modified digital camera and a RedEdge-M. | 23 |
| 1.9 | Orthomosaics obtained from aerial imagery. | 23 |
| 1.10 | Aerial imaging system implemented in a fixed-wing platform. | 24 |
| 1.11 | Fixed-wing platform used in [1] to produce a 2D and 3D model of a predefined area. | 25 |
| 1.12 | Hyperspectral imaging system used in [2]. | 25 |
| 1.13 | Quad-rotor for the implementation of an imaging system used in [3]. | 26 |

| | | |
|------|--|----|
| 1.14 | Platforms used for echohydrology application [4]. | 26 |
| 1.15 | Thermal imaging with a rotary-wing vehicle implemented in [5]. | 27 |
| 2.1 | Quad-rotor inertial and body frame. | 29 |
| 2.2 | Euler angles [6]. | 31 |
| 2.3 | Absorption spectra of chlorophyll and carotenoids. | 39 |
| 2.4 | Internal structure of a plant [7]. | 40 |
| 2.5 | Reflectance curves for vegetation at different stages [8]. | 41 |
| 2.6 | Reflectance curve of vegetation [8]. | 43 |
| 2.7 | Extended reflectance curve of vegetation [9]. | 44 |
| 3.1 | The overall aerial imaging system architecture. | 48 |
| 3.2 | Quad-rotor components equipped with the imaging system. | 49 |
| 3.3 | Cameras mounting rig developed in the LAB. | 51 |
| 3.4 | Mission Planner. | 52 |
| 3.5 | Quantum efficiency of the Aptina sensor. | 53 |
| 3.6 | Wratten 25 transmission curve. | 54 |
| 3.7 | Graphic representation of overlaps. | 56 |
| 3.8 | Elements that integrate the trigger system : flight controller, microcomputer and cameras. | 58 |
| 4.1 | Lenses of both cameras. | 62 |
| 4.2 | RGB image split into individual bands. | 63 |
| 4.3 | Near-infrared image split into the individual bands. | 64 |
| 4.4 | Histogram of the three bands of a near-infrared reflectance image. Horizontal axis represents pixel values (0 - 255) and vertical axis represents frequency of values. | 65 |
| 4.5 | NDVI computed with Fiji. | 66 |
| 4.6 | Flight trajectory generated by Mission Planner. | 67 |

| | | |
|------|---|----|
| 4.7 | Quad-rotor trajectory followed and points in space where the images are captured. | 68 |
| 4.8 | Images taken by the drone. | 70 |
| 4.9 | Multispectral orthomosaics. | 73 |
| 4.10 | NDVI of a soccer field computed by Fiji. | 74 |
| 4.11 | Manual trigger points on a park. | 75 |
| 4.12 | Orthomosaics of a park. | 76 |
| 4.13 | NDVI of a small area of a park computed by Fiji. | 77 |

List of Tables

| | | |
|-----|--------------------------------|----|
| 3.1 | Quad-rotor parameters. | 50 |
| 3.2 | Camera parameters. | 50 |

Acknowledgements

I would like to show my gratitude to Consejo Nacional de Ciencia y Tecnología (CONACYT) who brought me a Master scholarship, that was determinant in the development and continuity of my project. I also want to thank the Academic authorities of Centro de Investigaciones en Óptica (CIO) who economically supported me to participate in the International Conference on Unmanned Aircraft Systems this year. Similarly I am very thankful with my advisor, Dr. Gerardo Flores, for his continuous support.

Concerence papers

- Low-cost multi-spectral imagery system for crop monitoring. **A. Montes de Oca**, L. Arreola, A. Flores, J. Sanchez, G. Flores. International Conference on Unmanned Aircraft Systems 2018 (ACCEPTED).
- Improvement in the UAV position estimation with low-cost GPS and vision-based system: Application to a quad-rotor UAV. L. Arreola, **A. Montes de Oca**, A. Flores, J. Sanchez, G. Flores. International Conference on Unmanned Aircraft Systems 2018 (ACCEPTED).
- Nonlinear observer design for 1-DOF upper limb exoskeleton. Authors: J. Santis, A. Flores, **A. Montes de Oca**, L. Arreola and G. Flores. Conference on Decision and Control 2018 (UNDER REVIEW).
- Design of a simple controller for the flight mode transition of a hybrid drone. Authors: A. Flores, J. Sanchez, **A. Montes de Oca**, L. Arreola and G. Flores. Conference on Decision and Control 2018 (UNDER REVIEW).

Abstract

This work presents the design and development of a multispectral imaging system for crop monitoring tasks. The imaging system features two small digital cameras controlled by a microcomputer embedded in an Unmanned Aerial Vehicle (UAV) through a trigger system, which is specially designed for this purpose. One of the cameras has been modified to capture infrared radiation reflected by the vegetation. In order to determine the health status of the crops, the Normalized Difference Vegetation Index (NDVI) is computed in a developed software. Once the aerial imagery is obtained by the UAV, it is processed to eliminate image distortions and insert specific metadata needed for generating an orthomosaic with the health information of the plant or soil of interest. Finally, the vegetation index will be computed from the visible and infrared orthomosaics for a better interpretation of the user. Experiments are presented to show the effectiveness of the system.

Introduction

Precision agriculture requires data collection on weather, soil, crop's health and air quality in order to obtain preliminary analysis and predictive behavior of crops. The information gathered can be used to determine a set of preventive and corrective actions on crops that will improve farming management. These actions may be planting, watering, fertilizing and harvesting. The use of autonomous drones provides an overview of crop's health by collecting aerial imagery of an specific area. The use of Unmanned Aerial Systems (UAS) in precision agriculture applications has increased in the last three years. There is an important fact about this technology: it has been estimated that 80% of the sold drones from 2015 to 2025 will be used in this kind of applications [10]. This is mainly due to the UAS capability to provide to the farmers with important information related to crop management. Within the advantages of using UAS there is the low cost in comparison with manned aircraft or satellite-based systems. They also have the advantages of being small-sized and easy to use. All these facts promote the growing popularization of UAS in agriculture.

Aerial imaging is done using multi-rotor and fixed-wing UAS. Due to its aerodynamics, fixed-wing aircrafts can travel more distance than a quad-rotor with the same amount of power. This means a larger area coverage and also a larger amount of im-



Figure 1: The unmanned aerial vehicle used in this work. This drone is equipped with the proposed multispectral imagery system.

imagery collected. A quad-rotor instead, is more precise and easier to manipulate in smaller areas. This makes it ideal for testing on a lower scale.

Biological processes inside a plant's structure are related to certain spectral radiation that can be captured from the plants, specifically to the near-infrared radiation. So, multispectral image analysis and processing is able to provide useful information about biological characteristics of the vegetation, including health parameters. These kind of imagery can be digitally processed to determine the so-called *vegetation indices*. Currently, there are some multispectral imaging systems in the market ready to be implemented in diverse Unmanned Aerial Vehicles (UAV aka drones) platforms. It is important to mention that the cost of these systems may be expensive, also license software is sometimes needed to proceed analyze imagery obtained making it even more expensive.

To solve that problematic, an easy-to-implement and low-cost aerial imaging system has been developed with the use of a quad-rotor motorcraft and a dual camera system. With the use of the prototype shown in Fig. 1, aerial imagery was collected to generate orthomosaics and compute the Normalized Difference Vegetation Index (NDVI) from these images.

This thesis is organized as follows. Chapter 1 presents the previous and current

research done related to the work presented in this thesis. Chapter 2 includes fundamental knowledge related to the model of the quad-rotor and multispectral imagery. Chapter 3 offers an overview of the elements involved in the proposed system and how they contribute to aim the main objective of the project. In Chapter 4, the results are shown according to the experiments conducted following the methodology described in Chapter 3. Finally, in Chapter 5 it is summed up the conducted work, mentioning the achieved tasks, failures and future improvements.

CHAPTER 1

Literature review

1.1 Commercial multispectral imaging systems

Modern technology allows the development of specialized multispectral sensors useful in precision agriculture. Some of these sensors are able to capture specific wavelengths from the visible and part of non-visible spectrum. Systems dedicated to capture multispectral images are commonly able to capture blue (400 nm), green (500 nm), red (600 nm), red edge (740 nm) and specific near infrared bands (800 to 1100 nm) .

RedEdge-M multispectral camera is developed by MicaSense. It is one of the most popular commercial multispectral imaging system in the market. It has been designed to be equipped on UAV's to collect specialized imagery useful for precision agriculture monitoring tasks. The system is consists of a camera integrated by five monochromatic CCD sensors that simultaneously captures five discrete spectral bands. These bands are blue, green, red, red edge and near-infrared, enabling the creation of tailored indices for customized agriculture applications [11]. The Sentera Quad sensor is another multispectral camera available in the market. This device is similar to the RedEdge-M

provided by four CCD sensors. One sensor has a RGB Bayer filter, allowing the capture of a RGB image; the other sensors are monochromatic for three specific near-infrared wavelengths [12]. As third example, there is the ADC Lite designed and developed by Tetracam. This system allows the capture of green, red and three specific wavelengths of the near-infrared spectrum [13]. All these commercial systems have the capability to georeference images instantly which is useful when an orthomosaic is required. They also feature a manual trigger and a trigger interface with flight controller boards. Some of the multispectral imaging systems mentioned before are shown in Fig. 1.1.

RedEdge-M™
by MicaSense



(a) RedEdge-M.



(b) Sentera Quad.

Figure 1.1: Commercial multispectral imaging systems.

1.2 Aerial imaging system implementation and applications

Concerning the aerial imagery collection with UAV's, there is currently a high rate of research and development done. The type of aerial vehicles used, as well as imaging systems equipped, may vary according to the methodology and application proposed. According to [14], multispectral and hyperspectral imaging have several applications related to precision agriculture having each their own advantages and disadvantages. In [15], an imaging system has been developed using two low-cost hyperspectral sensors based on spectrometers as shown in Fig. 1.2. Both sensors are composed by their own optical system, GPS sensor and a data logger for a later georeferencing process.

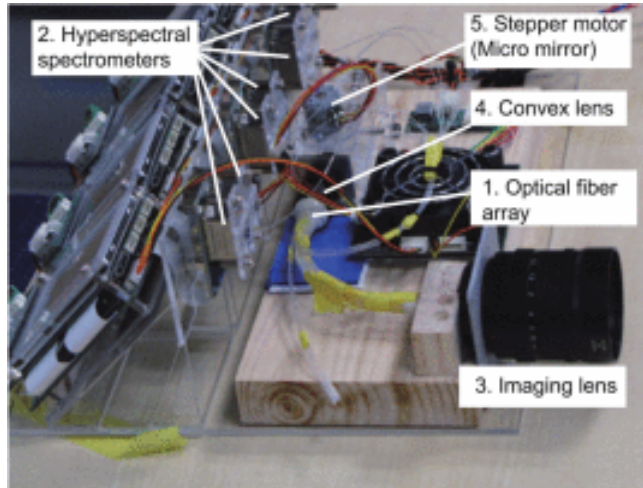


Figure 1.2: Spectrometer-based hyperspectral sensor.

Like most imaging systems, in [16] the authors have proposed an imaging system controlled by an on-board microcomputer that is able to insert GPS data into the metadata of the images taken. A dual-camera module compatible with the Raspberry P was used as the sensor device. One camera is sensitive to the visible spectrum while the other one is sensitive to the near-infrared spectrum. This is a light-weighted system designed for UAV implementation. In [17], a more complex imaging system has been developed using six CCD cameras each one with the addition of a specific filter. A Jetson TK1 microcomputer acts as the interface between the sensors and the flight controller. This microcomputer is also used for a faster response in the image processing during the flight. The Normalized Difference Vegetation Index (NDVI) is computed from the aerial imagery obtained.

Several studies have been focused to determine vegetation indices through multi-spectral imagery in order to understand the vegetation status. In [18] a relationship has been established between Stem Water Potential (SWP) and the NDVI of canopy through the analysis of multispectral aerial imagery. The purpose of this study is to manage water application rate treatment to an orchard. They use two Commercial-off-the-shelve (COTS) cameras Canon ELPH110HS to capture visible and near-infrared radiation from vegetation. Aerial imagery was taken with 75% of overlap at 60 m of

altitude. In [19], the model of the Leaf Area Index (LAI) and the NDVI are obtained from hyperspectral imagery. In [20], a comparison has been done between a commercial and a modified digital cameras. Green Normalized Difference Vegetation Index (GNDVI) is computed with imagery collected from both cameras. Chlorophyll content is also estimated using the triangular Greenness Index (TGI). In [21], a chlorophyll map has been created from aerial hyperspectral imagery. Agisoft Photoscan software has been used for the image processing.

The use of rotorcraft vehicles in these kind of applications is vastly used due to the easy incorporation of imaging devices in these platforms. Next will be mentioned several imaging systems tested on rotary-wing UAV's. In [22], an assessment of crop damage by hailstorm in potatoes has been made using aerial imagery provided by a quad-rotor. This study has been made obtaining and analyzing the Green Normalized Difference Vegetation Index (GNDVI). A NiteCanon ELPH110 camera has been used in this research. Modifying the camera, the blue band was made more sensitive to near-infrared radiation. The image processing is done with MATLAB. In [23], stress detection in a citrus orchard has been made with an aerial imaging system composed by two cameras. One camera is a XNite Canon SX230 intended to capture green, blue and near-infrared radiation. The second camera is a Tetracam model; MATLAB is used for the image processing. The GNDVI is computed using both cameras and obtained data is compared. In [24], multispectral and hyperspectral imaging systems has been proposed to collect imagery to compute the NDVI. Spectrometer-based cameras were used as hyper-spectral sensors. Three cameras were used as multispectral sensors. One camera captured a RGB image while the other two are used to capture near-infrared and red edge radiation. In [25], a dual-SLR camera system has been used to obtain multispectral imagery. One camera has been modified to be sensitive to near-infrared radiation so, RGB plus a near-infrared band can be captured by the system. The flight trajectories were created with GeoScan Planner which is mission planning software. AgiSoft PhotoScan was used to create the orthomosaics from the aerial imagery. The analysis of the images led to the color characteristics of the vegetation obtained using

a specialized algorithm proposed by the authors. In [26], a multispectral camera is attached to an UAV for wheat cultivar monitoring. The NDVI was computed from imagery obtained from a RedEdge-M. Mission Planner was used to plan the flight trajectories performed; overlaps used were 70% and 80%. In [27], a multispectral camera system has been developed by the authors using one camera compatible with the Raspberry Pi. Multispectral imagery was obtained through a set of interchangeable external filters over the camera as in Fig. 1.3.

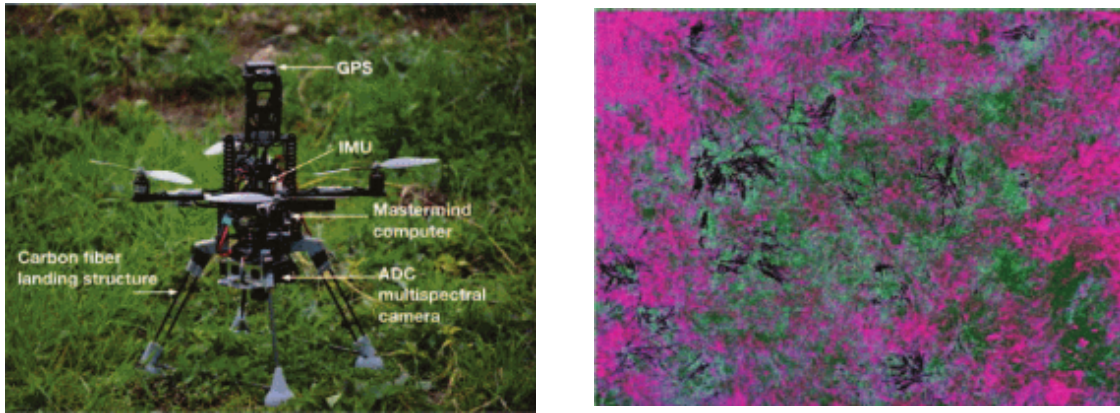


Figure 1.3: Imaging system with external filters.

A different method to obtain multispectral imagery has been proposed in [28] where a consumer camera is modified adding a blue gel filter. The modification of the camera using the blue filter allows the camera to keep the red sensitivity in the red band and makes the blue band to be more sensitive to near-infrared radiation. In [29], an ADC Lite camera is equipped on a quad-rotor to collect imagery for the computation of the NDVI. Flight tests were made at 7 meters of altitude. Images taken are georeferenced to generate orthomosaics of the covered area. The image matching by features is developed by the authors and then compared with the commercial software Pix4D. Fig. 1.4 shows the UAV used and the NDVI obtained.

In [30], a Condor-1000 MS5 5 CCD multi-channel is used as the imaging sensor to collect aerial imagery on a single rotary-wing vehicle. Collected imagery is used to compute the NDVI. Fig. 1.5 shows the UAV used and the computed NDVI.

In [31], a complete imaging system has been developed integrated by a thermal camera and a Tetracam camera controlled by a microcomputer. The camera trigger



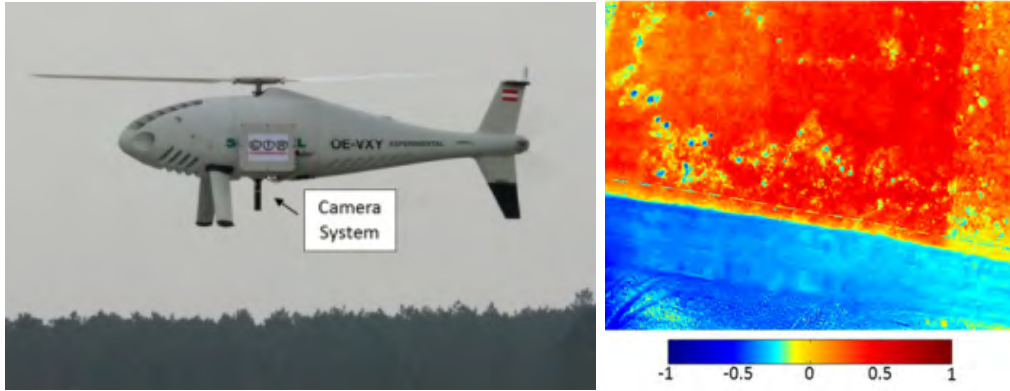
(a) Description of the imaging system mounted on a quad-rotor.

(b) NDVI.

Figure 1.4: Implementation of a multispectral imaging system for NDVI computation.

is performed according to specific way-points in the flight plan. GPS data of trigger points is stored in the images metadata. The photogrammetric parameters used for the orthomosaic generation are 75% for end lap and 60% for side lap at 100 meters of altitude. Later image processing is made with Agisoft PhotoScan. The Crop Water Stress Index (CWS) and the NDVI were obtained from the aerial imagery collected. Chlorophyll map was also obtained computing the Gitelson-erzlyak index. In [32], a lightweight hyperspectral imaging system has been developed on a octa-rotor as in Fig. 1.6. The intended weight of the system is 2 Kg. The system consists in a spectrograph, a camera, a GPS unit, a microcomputer and a frame grabber. Images obtained were aligned into an orthomosaic with Agisoft Photoscan Pro software.

In [33], a multispectral camera is attached to an UAV in order to obtain NDVI from multispectral imagery of a vineyard according to the experiments reported. Spectral data obtained from the camera is compared with ground data obtained from a spectrometer. The multispectral sensor used is the Tetracam ADC-lite camera. Pictures were taken every 5 seconds at 150 meters of altitude. In [34], an hyperspectral imaging system that does not require reference ground targets for reflectance calibration has been proposed. This system is composed by a Samsung NX300 digital camera, and a



(a) Rotary-wing vehicle.

(b) NDVI.

Figure 1.5: Multispectral imaging system implemented in a rotary-wing vehicle.



Figure 1.6: Hyperspectral imaging system implemented on a octa-rotor.

spectrometer. A microcomputer is also equipped to trigger the camera and store GPS data of trigger points. A Pixhawk autopilot is used to perform the flights. Flight tests were made at 100 meters of altitude with 75% of end lap and 65% of side lap.

Multi-rotor platforms are not only used for index computation, they are also used for 3D reconstruction as in [35], where a low-cost imaging system designed by the authors has been proposed using a Pixhawk autopilot as flight controller and a Canon PowerShot S100 camera. Imagery collected is processed using Pix4D for 3D surface modeling. In [36], 3D modeling of wetlands is done for delineation and classification. Images are taken with 80% of overlap at 120 meters of altitude. Structure-from-Motion (SfM) computer vision techniques are used to derive ultra-high resolution point clouds, orthophotos and 3D models from the multi-view photos taken with the UAV. Image processing is made with Agisoft PhotoScan software.

Instead of using multi-rotor platforms, many applications used fixed-wing UAV's. The use of these kind of platforms allows to cover larger areas. The following researches are implemented in these kind of aerial vehicles. In [37], two Panasonic cameras were used to obtain the NDVI. Flight tests are performed at 122 meters of altitude and 80% of overlap. Agisoft PhotoScan is used to correct the images. In [38], multispectral imagery obtained by the UAV is analyzed to estimate chlorophyll content in plants. Two Canon S-95 cameras and a Thermal camera are used. One of the Canon cameras was modified to be sensitive to near-infrared radiation. EnsoMOSAIC was used to generate the orthomosaics. A chlorophyll meter was used to establish a relationship between multispectral imagery and corresponding measures. This led to chlorophyll estimation. In [39], a system designed to collect georeferenced aerial imagery featuring a GhostFinger camera was developed. This device can be triggered externally with another device, and also be coupled with a GPS module to georeference images when are taken. gRAID and World Wind were used to do the image processing. The platform used in that work is shown at Fig1.7.

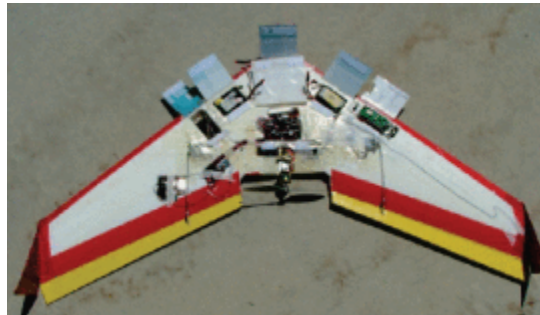


Figure 1.7: Imaging system implemented in a fixed-wing UAV platform.

In [40], a low-cost multispectral imaging system is developed using a Canon S100. A dual-band filter is added to the camera to allow the capture of red and near-infrared wavelengths. Results obtained with the camera were compared with results obtained with a RedEdge-M as is shown in Fig 1.8. Experiments were made over an apple orchard with an altitude of 94 meters.

In [41], another multispectral aerial imaging system has been developed featuring

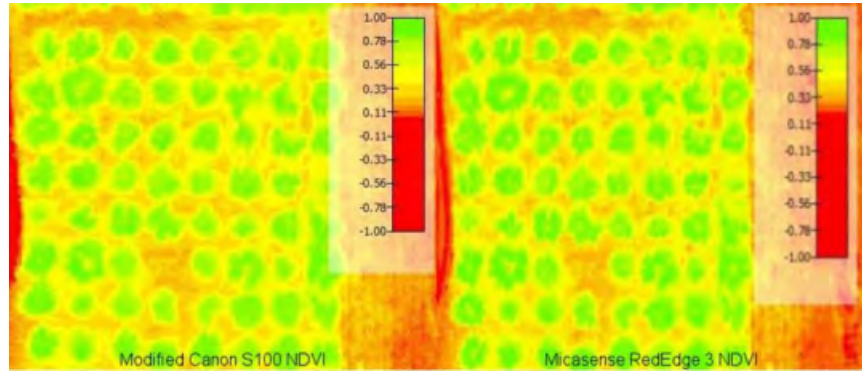
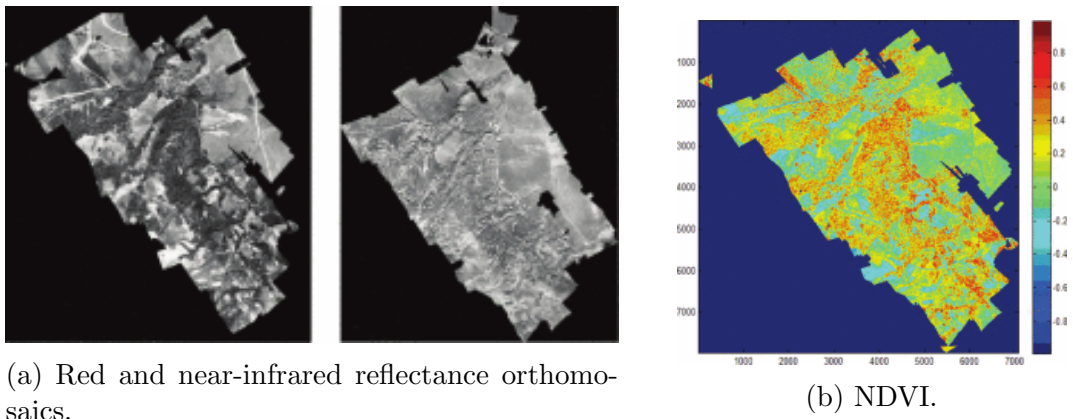


Figure 1.8: NDVI obtained with a modified digital camera and a RedEdge-M.

Point Gray Chameleon cameras and a fixed-wing UAV. The system is able to collect aerial imagery according to trigger events commanded by the flight controller. Images are taken and georeferenced during flight with the use of a microcomputer. Cameras are monochromatic containing each one a customized filter, allowing the capture of visible and a near-infrared reflectance images. Pixhawk autopilot was used as flight controller. Mission planner was used to plan the flight trajectory with overlaps of 75%. Pix4D was used to generate the required orthomosaics. To align both images, a set of control points were selected to generate a transformation function between the two images. Then the NDVI was calculated from these images. Fig. 1.9a shows both orthomosaics while Fig. 1.9b shows the computed NDVI.



(a) Red and near-infrared reflectance orthomosaics.

(b) NDVI.

Figure 1.9: Orthomosaics obtained from aerial imagery.

3D mapping is also made by fixed-wing platforms as in [42], where it is shown the

design and construction of an aerial imaging system for 3D reconstruction. The UAV system is composed by a 3DR Robotics autopilot. A digital camera Sony NEX 7 is mounted on the drone and the trigger is controlled by the flight controller through an IR trigger device. The trajectory was planned using Mission Planner with an overlap of 75% between images and flight lines. Reconstruction was obtained by using Pix4D. The system can be seen at Fig 1.10.

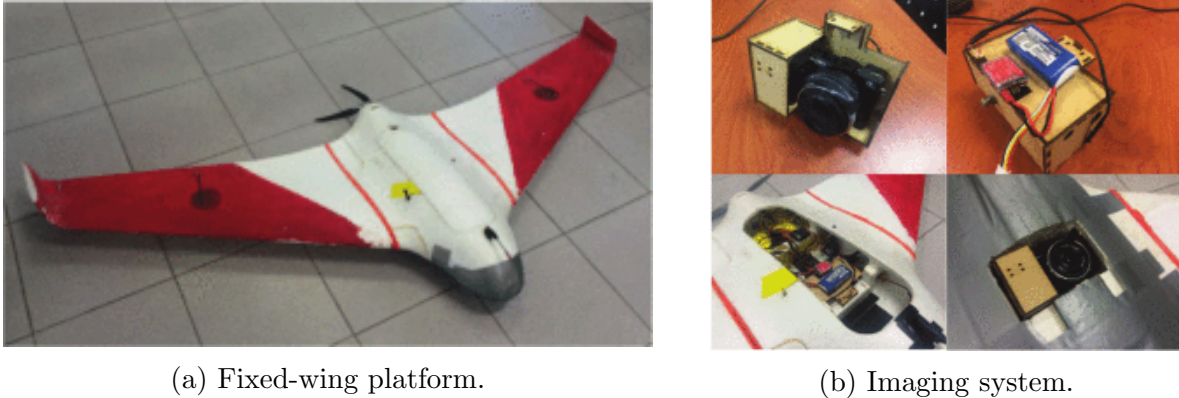


Figure 1.10: Aerial imaging system implemented in a fixed-wing platform.

In [1], a low-cost system is developed to produce a 2D and 3D model of the area covered by the UAV shown in Fig. 1.11. A Sony NEX-6 DSLR is used as the imaging sensor. The trigger was performed through an IR shutter. Images were georeferenced using the coordinates of the trigger points stored in the log file of the flight. Agisoft photoscan was used for image processing. Mission Planner was used to plan the trajectories. The altitude of the flights was set to 80 meters of altitude and overlaps of 80% and 60%.

In [43], an imaging system to map and monitor sand dunes and beaches was developed using the SenseFly platform. The camera used is the Canon Ixus 220 HS. Mission was planned using the eMotion software package that was provided by the platform. Using Agisoft Photoscan, the images obtained were corrected and processed to extract point clouds and build a surface model and orthomosaics.

There are some researchers that use multiple UAV platforms to implement their imaging applications. Next will be mentioned some cases. In [44], aerial imagery has

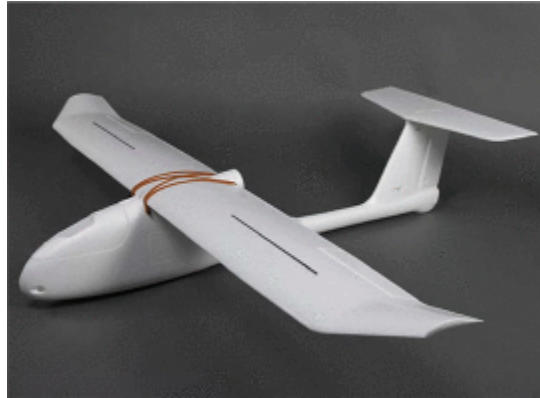


Figure 1.11: Fixed-wing platform used in [1] to produce a 2D and 3D model of a predefined area.

been obtained using both fixed-wing and a rotary-wing UAVs. The main objective was to map the terrain at 300 and 100 meter of altitude, respectively. The camera equipped on the plane is a Pentax Optio. The camera equipped on the multi-rotor is a Sony Alpha NEX-5N. Flights were conducted with 60% and 30% of overlap. Using similar platforms, in [2], multispectral and hyperspectral imaging systems were developed using a MT9P031 Aptina CMOS sensor and a Fabry-Perot interferometer-based as imaging sensors, respectively. Flight tests were conducted at 150 meters of altitude with 70% and 80% of overlap. Fig. 1.12 shows the Fabry-Perot interferometer-based sensor used as hyperspectral sensor.

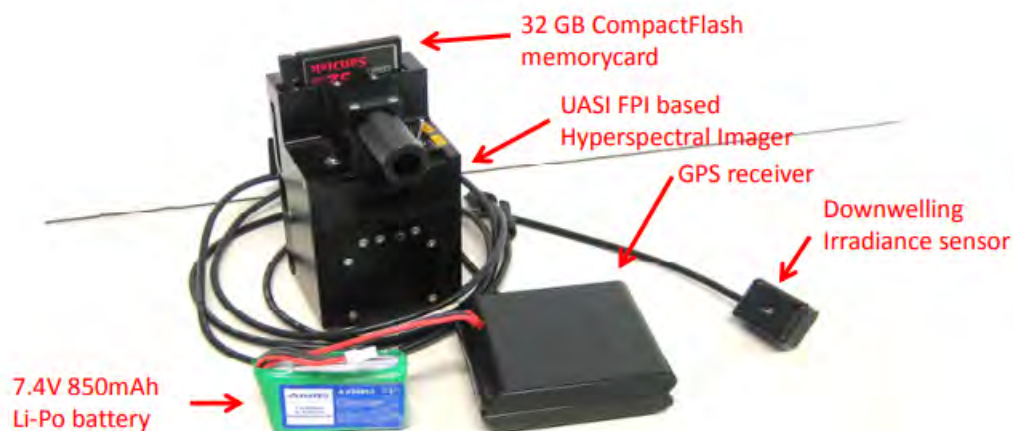


Figure 1.12: Hyperspectral imaging system used in [2].

In [3], a Vertical-Take-Off and Landing (VTOL) multi-rotor and a fixed-wing platform were used to test the implementation of aerial imaging systems. A camera module compatible with a Raspberry Pi was equipped on the multi-rotor. On the fixed-wing, a GoPro camera was used. Data obtained was stored in the microcomputer. The quad-rotor used in this research is shown at Fig. 1.13



Figure 1.13: Quad-rotor for the implementation of an imaging system used in [3].

In [4], rotary-wing and fixed-wing UAVs were used for echohydrology model predictions by performing aerial imaging. The sensing devices used on the fixed-wing were: a Canon SD900, a Tetracam camera and a FLIR thermal camera. On the rotary-wing a Canon EOS5D, a FLIR thermal camera and a Hero HD camera were used. The UAVs used are shown at Fig. 1.14.

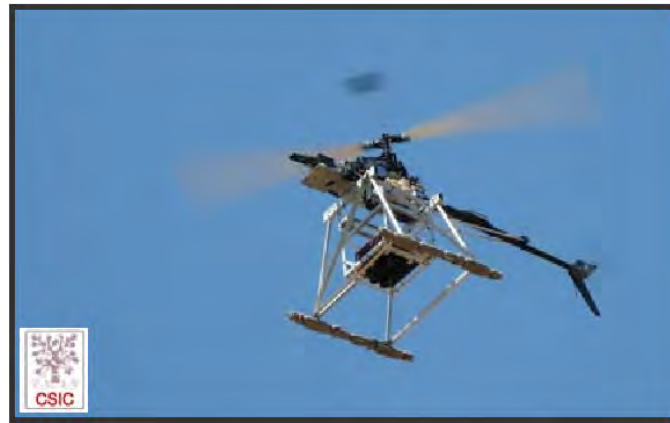


(a) Fixed-wing platform. (b) Rotary-wing platform.

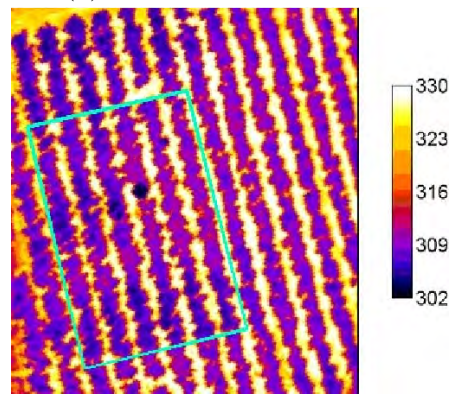
Figure 1.14: Platforms used for echohydrology application [4].

In [5], two platforms were developed for multispectral and thermal imaging purposes.

The first is a rotary-wing and the other is a fixed-wing. As imaging sensors, two devices were used: a) a MCA-6 from Tetracam with 6 individual sensors and interchangeable filters, and b) the thermal Thermovision A40M camera. Some indices were computed from the aerial imagery collected such as: the NDVI, Leaf Area Index (LAI), and Photochemical Reflectance Index (PRI). The UAV used and results are shown in Fig. 1.15



(a) Rotary-wing platform.



(b) Thermal image.

Figure 1.15: Thermal imaging with a rotary-wing vehicle implemented in [5].

2.1 Introduction

UAVs, specially quad-rotors, are controlled using electronics control systems and sensors. They are composed by several elements: a frame, Electronic Speed Controllers (ESC's), motors, propellers, a battery, a flight controller and an Inertial Measurement Unit (IMU). IMU is used to get the current information of quad-rotor attitude consisting of a 3-axis accelerometer, gyroscope and magnetometer. The combination of the IMU and an on-board processing system is known as Attitude Heading Reference System (AHRS) [45]. The GPS module gets the quad-rotor absolute position. Other components as the barometer, ultrasonic and infrared sensors are used to determine the absolute altitude. Quad-rotors can be equipped with any kind of camera for vision and mapping applications.

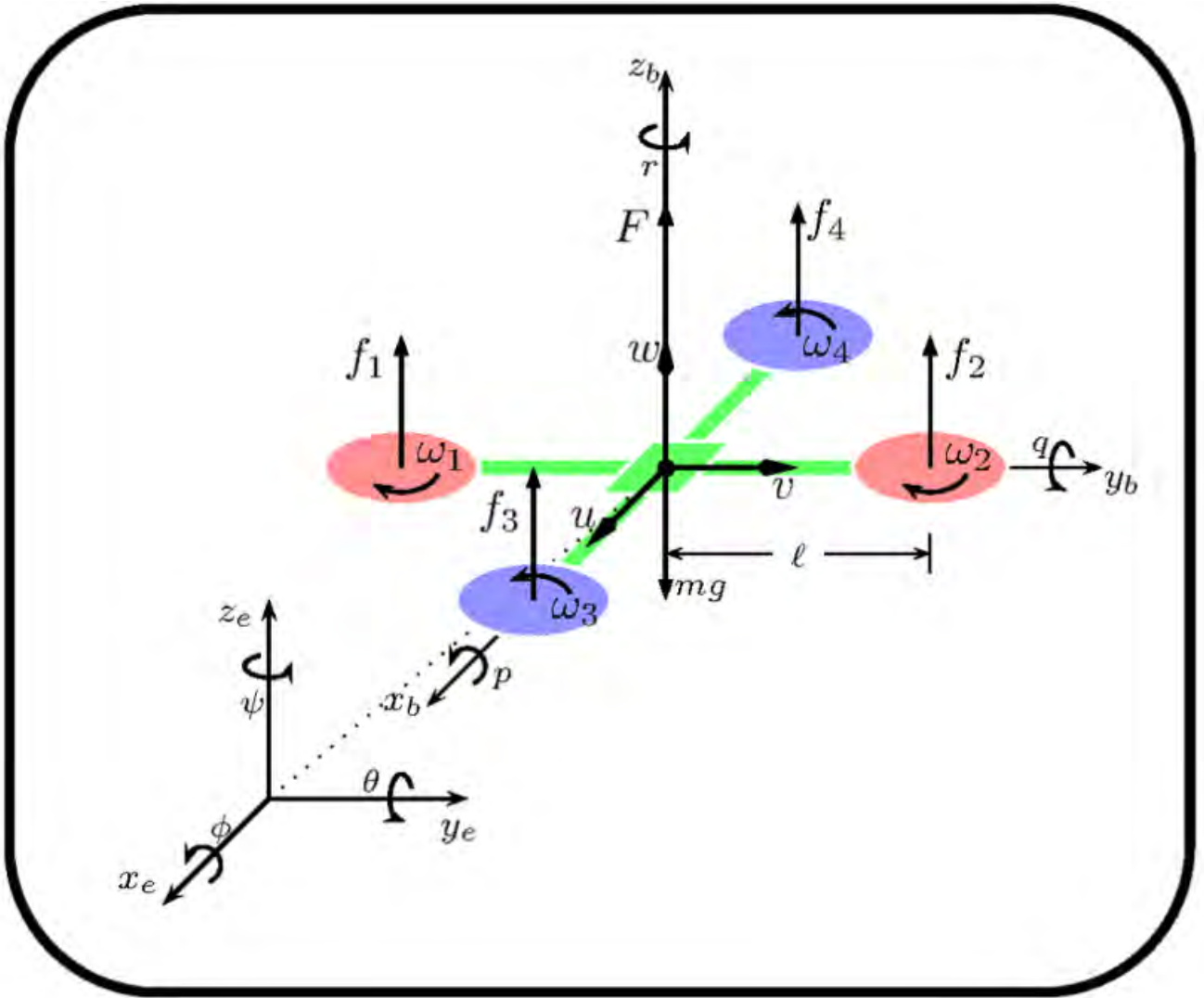


Figure 2.1: Quad-rotor inertial and body frame.

2.2 Quad-rotor Model

If a quad-rotor is considered as a rigid body, their dynamics can be explained using Newton-Euler equations. According to Fig. 2.1, each propeller rotates at an angular velocity ω_i producing a corresponding force f_i directed upwards and a counteracting torque τ_i directing at the opposite direction to the direction of rotation¹. The propellers with angular speed ω_1 and ω_2 spin clockwise while the other two spin counter-clockwise,

¹Here $i = 1, 2, 3, 4$ represents each propeller

see Fig. 2.1. Attitude and position, i.e. pose, of the vehicle can be reached by varying the thrust of an specific rotor. The four rotors generate their corresponding angular velocity, torque and force.

2.2.1 Airspeed and groundspeed

Considering that the vehicle is always located in the air, the velocity of the vehicle with respect to the surrounding air is denoted as V_a , and the ground speed, represented by the velocity with respect to the inertial frame is denoted as V_g . These velocities are related as follows

$$V_a = V_g - V_w \quad (2.1)$$

Where V_w is the wind velocity relative to the inertial frame. The aircraft velocity V_g can be expressed in the body frame in terms of its components along the i^b, j^b and k^b axes as

$$V_g^b = \begin{bmatrix} u_i \\ v_j \\ w_k \end{bmatrix} \quad (2.2)$$

Where V_g^b is the velocity of the aircraft with respect to the inertial frame, as expressed in the body frame.

2.2.2 Euler equations

Euler angles represent a sequence of three elemental rotations as in Fig. 2.2. Since any orientation can be achieved by composing three elemental rotations. These rotations start from a known standard orientation. The combination used is described by the following rotation matrices as in [6]:

$$R(\psi) = \begin{bmatrix} \cos \psi & \sin \psi & 0 \\ -\sin \psi & \cos \psi & 0 \\ 0 & 0 & 1 \end{bmatrix} \quad (2.3)$$

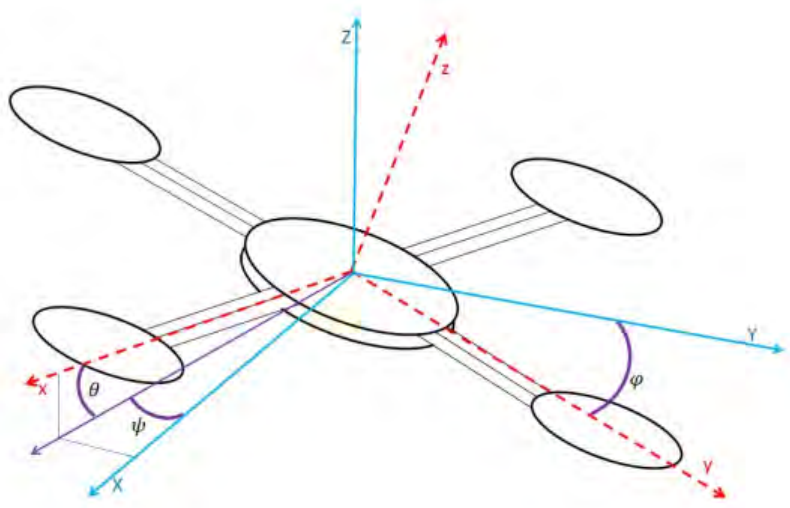


Figure 2.2: Euler angles [6].

$$R(\theta) = \begin{bmatrix} \cos \theta & 0 & -\sin \theta \\ 0 & 1 & 0 \\ \sin \theta & 0 & \cos \theta \end{bmatrix} \quad (2.4)$$

$$R(\varphi) = \begin{bmatrix} 1 & 0 & 0 \\ 0 & \cos \varphi & \sin \varphi \\ 0 & -\sin \varphi & \cos \varphi \end{bmatrix} \quad (2.5)$$

So, the inertial position coordinates and the body reference coordinates are related by the rotation matrix obtained from computing

$$R(\varphi, \theta, \psi) = R(\varphi)R(\theta)R(\psi) \quad (2.6)$$

Substituting (2.3), (2.4) and (2.5), the rotation matrix is now defined as

$$R(\varphi, \theta, \psi) = \begin{bmatrix} C_\theta C_\psi & C_\theta S_\psi & -S_\theta \\ S_\varphi S_\theta C_\psi - C_\varphi S_\psi & S_\varphi S_\theta S_\psi + C_\varphi C_\psi & S_\varphi C_\theta \\ C_\varphi S_\theta C_\psi + S_\varphi S_\psi & C_\varphi S_\theta S_\psi - S_\varphi C_\psi & C_\varphi C_\theta \end{bmatrix} \quad (2.7)$$

were C_* and S_* are the abbreviation of $\cos(*)$ and $\sin(*)$, respectively.

The first group of kinematic equations need to express translational velocity in terms of velocity components in the body frame. The aircraft position vector \mathbf{p} has its components p_x , p_y , and p_z located in the frame F^I while velocity components from (2.2) are expressed in frame F^b . To relate these two groups of variables, a time differentiation and a rotational transformation need to be applied as shown below:

$$\frac{d}{dt} \begin{bmatrix} p_x \\ p_y \\ p_z \end{bmatrix} = R(\varphi, \theta, \psi) \begin{bmatrix} u \\ v \\ w \end{bmatrix} = R(\varphi, \theta, \psi)^{-1} \begin{bmatrix} u \\ v \\ w \end{bmatrix} \quad (2.8)$$

Due to the time derivative of position in the inertial frame F^I , a rotation R_b^v needs to be used in (2.8) in order to obtain velocity components with respect to the inertial frame F^I , so the inverse of (2.7) must be replaced. Substituting these matrix, position vector is expressed as in [46] as:

$$\begin{bmatrix} \dot{p}_x \\ \dot{p}_y \\ \dot{p}_z \end{bmatrix} = \begin{bmatrix} C\theta C\psi & S\varphi S\theta C\psi - C\varphi S\psi & C\varphi S\theta C\psi + S\varphi S\psi \\ C\theta S\psi & S\varphi S\theta S\psi + C\varphi C\psi & C\varphi S\theta S\psi - S\varphi C\psi \\ -S\theta & S\varphi C\theta & C\varphi C\theta \end{bmatrix} \begin{bmatrix} u \\ v \\ w \end{bmatrix} \quad (2.9)$$

Another relationship that need to be defined is the one between the angular positions: ψ , θ , and φ ; and the angular rates: p , q , and r . The time derivatives of angular positions are not equal to the angular rates because these two groups of variables are expressed in different coordinate frames. The Euler angles are defined subsequently along three different coordinate frames while the angular rates are defined in the body frame [46]. To obtain the equation that relates Euler angles and angular rates, angular rates need

to be expressed as

$$\begin{bmatrix} p \\ q \\ r \end{bmatrix} = \begin{bmatrix} \dot{\varphi} \\ 0 \\ 0 \end{bmatrix} + R(\varphi) \begin{bmatrix} 0 \\ \dot{\theta} \\ 0 \end{bmatrix} + R(\varphi)R(\theta) \begin{bmatrix} 0 \\ 0 \\ \dot{\psi} \end{bmatrix} \quad (2.10)$$

Roll angle is already defined in body frame so it does not need a rotation. Pitch and yaw angles need an appropriate rotation so they can be defined in the body frame, so $R(\varphi)$, and $R(\theta)$ need to be substituted to obtain a simplified expression as follows

$$\begin{bmatrix} p \\ q \\ r \end{bmatrix} = \begin{bmatrix} 1 & 0 & -\sin \theta \\ 0 & \cos \varphi & \sin \varphi \cos \theta \\ 0 & -\sin \varphi & \cos \varphi \cos \theta \end{bmatrix} \begin{bmatrix} \dot{\varphi} \\ \dot{\theta} \\ \dot{\psi} \end{bmatrix} \quad (2.11)$$

Multiplying both sides in (2.11) by the inverse matrix and rearranging the equation, expressions for the derivatives of the angular positions can be found in terms of angular positions and angular rates in the next equation:

$$\begin{bmatrix} \dot{\varphi} \\ \dot{\theta} \\ \dot{\psi} \end{bmatrix} = \begin{bmatrix} 1 & \sin \varphi \tan \theta & \cos \varphi \tan \theta \\ 0 & \cos \varphi & -\sin \varphi \\ 0 & \sin \varphi \sec \theta & \cos \varphi \sec \theta \end{bmatrix} \begin{bmatrix} p \\ q \\ r \end{bmatrix} \quad (2.12)$$

2.2.3 Newton equations

The rotational motion equation of the aircraft can be obtained using Newton's second law obtaining the time derivative of angular momentum as expressed next:

$$\dot{\vec{H}} = \vec{M} \quad (2.13)$$

where \vec{M} is the total external moment acting on the center of mass and \vec{H} is the angular momentum. Classically, the angular momentum vector \vec{H} is defined as the

cross-product of the position vector \vec{r} and the momentum vector \vec{p} as:

$$\vec{H} = \vec{r} \times \vec{p} \quad (2.14)$$

Moment \vec{H} can be expressed as its vector form as:

$$\vec{H} = \begin{bmatrix} H_x \\ H_y \\ H_z \end{bmatrix} = \begin{bmatrix} yp_z - zp_y \\ yp_x - zp_z \\ yp_y - zp_x \end{bmatrix} \quad (2.15)$$

The expression for angular momentum that describes the rate of change with respect of time of a rigid body about its center of mass is given by:

$$\dot{\vec{H}} = \sum_i \vec{r}_i \times m_i \dot{\vec{r}}_i \quad (2.16)$$

Where r_i is the position vector of a particle m_i . In this case, the position of all the particles are fixed in the body, so the velocity of each particle is defined by:

$$\dot{\vec{r}}_i = \vec{\omega} \times \vec{r}_i \quad (2.17)$$

As it is already know, $\vec{\omega}$ is the body angular velocity. In this case the body is the quadrotor, hence it is assumed that it has a continuous mass distribution, so the particle mass can be represented by its density times an elemental volume ρdV . So now, the expressions of velocity and elemental volumes can be substituted, thus the summation expression in (2.16) can be replaced by an integral as follows:

$$\vec{H} = \int_v \rho \vec{r} \times (\vec{\omega} \times \vec{r}) dV \quad (2.18)$$

where \vec{r} is expressed as:

$$\vec{r} = x\hat{i} + y\hat{j} + z\hat{k} \quad (2.19)$$

On the other hand, the vector cross product can be defined as:

$$\vec{r} \times (\vec{\omega} \times \vec{r}) = [(y^2 + z^2)p - xyq - xzr]\hat{i} + [(x^2 + z^2)q - yxp - yzr]\hat{j} + [(x^2 + y^2)r - zxp - zyq]\hat{k} \quad (2.20)$$

Using the previous equations, we can define the moments of inertia as:

$$\begin{aligned} I_{xx} &= \int_v \rho(y^2 + z^2) dv \\ I_{yy} &= \int_v \rho(x^2 + z^2) dv \\ I_{zz} &= \int_v \rho(x^2 + y^2) dv \\ I_{xy} &= I_{yx} = \int_v \rho(xy) dv \\ I_{xz} &= I_{zx} = \int_v \rho(xz) dv \\ I_{yz} &= I_{zy} = \int_v \rho(yz) dv \end{aligned} \quad (2.21)$$

It is assumed that the four arms of the quad-rotor are symmetric and are aligned with the x and y axes. This leads to a diagonal inertia matrix, which is a diagonal matrix I where I_{xx} and I_{yy} are equal.

$$\begin{bmatrix} I_{xx} & 0 & 0 \\ 0 & I_{yy} & 0 \\ 0 & 0 & I_{zz} \end{bmatrix} \quad (2.22)$$

This leads to determine the equations of the particles m_i of the system, that are defined by [6] as follows:

$$\begin{aligned} m_x &= \dot{p}I_x - qrI_y + qrI_z \\ m_y &= \dot{q}I_y + prI_x - prI_z \\ m_z &= \dot{r}I_z - pqI_x + pqI_y \end{aligned} \quad (2.23)$$

From the Newton equation we have:

$$\vec{F} = m\dot{\vec{v}} \quad (2.24)$$

where \vec{F} is defined as the total external force acting on the quad-rotor, \vec{v} is the absolute velocity of the center of mass and m is the mass of the quad-rotor [47]. The vector \vec{F} can be expressed in terms of the x , y and z components as:

$$\vec{F} = F_x \hat{i} + F_y \hat{j} + F_z \hat{k} \quad (2.25a)$$

And velocity vector is defined as in (2.2) as:

$$\vec{v} = u \hat{i} + v \hat{j} + w \hat{k} \quad (2.25b)$$

The quad-rotor is rotating with angular velocity, the absolute acceleration can be expressed as:

$$\dot{\vec{v}} = \dot{\vec{v}}_b + \vec{\omega} \times \vec{v} \quad (2.26)$$

where $\dot{\vec{v}}_b$ is the acceleration seen from the body axis. This term and the angular velocity can also be described in terms of a vector form as:

$$\begin{aligned} \dot{\vec{v}}_b &= \dot{u} \hat{i} + \dot{v} \hat{j} + \dot{w} \hat{k} \\ \vec{\omega} &= p \hat{i} + q \hat{j} + r \hat{k} \end{aligned} \quad (2.27)$$

Expanding the cross product in (2.26), the equation results in:

$$\vec{\omega} \times \vec{v} = \hat{i}(wq - vr) - \hat{j}(wp - ur) + \hat{k}(vp - uq) \quad (2.28)$$

Considering force components in (2.25a) with gravitational force terms, the three force components can be written as follows:

$$F = \begin{bmatrix} F_{x-applied} - mg \sin(\theta) \\ F_{y-applied} + mg \cos(\phi) \\ F_{z-applied} + mg \cos(\theta) \cos(\phi) \end{bmatrix} \quad (2.29)$$

Also we can express each term of (2.25a) using (2.28) in (2.24) as follows:

$$\begin{aligned}
 F_x &= m(\dot{u} + wq - vr) \\
 F_y &= m(\dot{v} + wp - ur) \\
 F_z &= m(\dot{w} + vp - uq)
 \end{aligned}
 \tag{2.30}$$

Finally the quad-rotor equations of motion are given by (2.30), (2.9) and (2.12).

2.3 Multispectral properties of vegetation

The health status of vegetation can be determined by analyzing and comparing specific radiation reflected by plants. This method allows to determine whether a plant is dry, stressed or healthy. Available spectrum reflected by a plant that can be sensed by electronic sensors is ranged from the visible spectrum to the thermal spectrum. Specific wavelengths within this range of electromagnetic radiation is bounded to certain characteristics of the plant. In this section, the relationship between health status and radiation reflected by a plant will be explained.

2.3.1 Optical aspect of photosynthesis and its relationship with vegetation stress

As mentioned, health status of a plant can be identified thanks to an interesting relationship that exists between vegetation stress and photosynthesis. Photosynthesis is a biochemical process carried out mostly by plants to convert light energy naturally from the sun, into chemical energy that can be later released to fuel the organisms activities. The chemical energy generated is stored in carbohydrate molecules, such as sugars, which are synthesized from carbon dioxide and water. In most cases, oxygen is a by-product released [48]. This process always begins when energy from light is absorbed by proteins called reaction centers that are held inside organelles called chloroplasts. Chloroplasts are most abundant in leaf cells and contain green chlorophyll pigments.

Chlorophyll is a pigment that allows light absorption in a plant. There are two types of chlorophyll which absorb different spectra of light: Chlorophyll A and B.

Chlorophyll A is the most common photosynthetic pigment. It naturally has an excellent visible light absorption property [49]. In this spectrum, chlorophyll tends to absorb violet, blue and red wavelengths while green wavelengths are reflected. This can be noticed as plants are mostly green to our eyes. Chlorophyll participates mainly in oxygenic photosynthesis in which oxygen is the main by-product of the process. All oxygenic photosynthetic organisms contain this type of chlorophyll. Similarly, chlorophyll B primarily absorbs blue light and is used to complement the absorption spectrum of chlorophyll A by extending the range of light wavelengths that a photosynthetic organism is able to absorb. Both of these types of chlorophyll allow maximum absorption of light in the blue and red spectrum.

Carotenoids are another pigments in plants that also absorbs light, but dont produce energy themselves. They must pass that energy onto the chlorophyll, then it can utilize that energy to create carbohydrates. Carotenoids also provide protective properties to plant cells that help protect the plant from elements such as ultra-violet light. Fig. 2.3 shows the absorbance spectrum for chlorophyll and carotenoids. It can be seen that indeed, the main light absorbance due to photosynthesis occurs around blue and red wavelengths.

Considering the previous information, monitoring chlorophyll will help determining the productivity of the plant [50]. The productivity of a plant can be affected by many stress factors, such as drought, which is a stress factor that affects primarily the photosynthetic activity in plants. This, due to the chlorophyll level reduction in the plant [51]. A change in chlorophyll content is one of the most common symptoms of plant stress. So, that is the reason why photosynthesis is strongly attached to the health of a plant. However, chlorophyll does not last for a long time. In the autumn or winter months, leaves in the plants start changing colors from green into shades of gold, brown, red, and burgundy. This happens due to the lack of chlorophyll content letting the carotenoids pigments become visible.

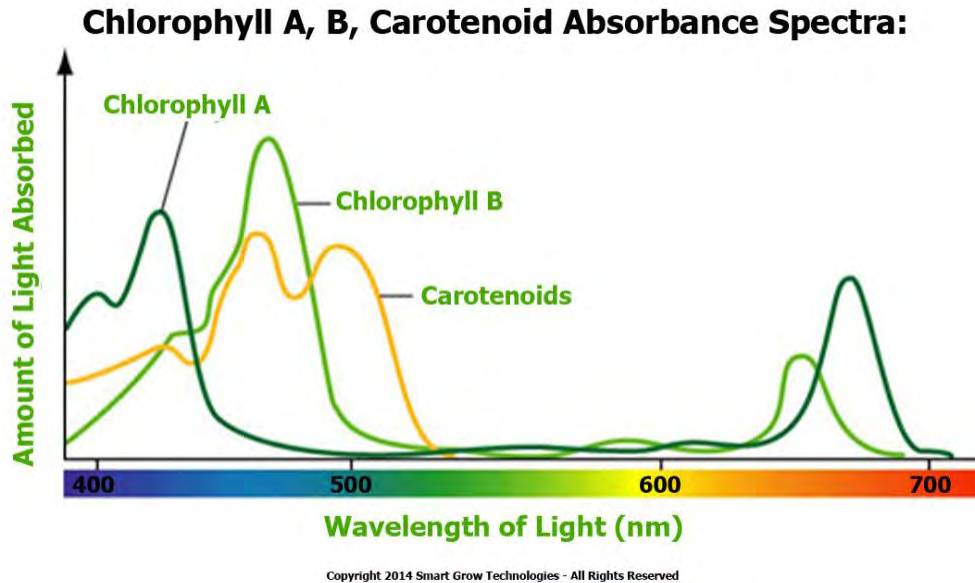


Figure 2.3: Absorption spectra of chlorophyll and carotenoids.

In common green leaves, photosynthesis occurs in two types of mesophyll cells: those in palisade tissue and those in sponge tissue. Palisade and sponge tissue cells contain chloroplasts, and chloroplasts contain chlorophyll. Palisade tissue cells, which face toward the upper surface, generally contain more chloroplasts than sponge tissue cells. Therefore, the upper surface of the leaf is greener than the lower surface. When a leaf is exposed to sunlight, the biochemical molecules in the mesophyll cells will absorb some wavelengths. This absorption results in a high-energy state, or excited state. Based on the different molecular absorption or reflection characteristics of the biochemicals, their concentrations in leaves can be deduced from the leaves reflection spectra. The sponge tissue in leaves controls the amount of energy reflected by the near-infrared reflection. Sponge tissue lies below the palisade tissue and consists of cells and intercellular spaces. Oxygen and carbon dioxide exchange here during the photosynthesis. The large amount of near-infrared energy that is reflected by leaves is due to multiple scattering between cell walls and air gaps [52]. Fig. 2.4 shows the internal structure of a leaf.

Concerning the near-infrared spectrum, wavelengths near 700 nm related to reddish hues are also crucial for plant stress detection and the estimation of leaf chlorophyll

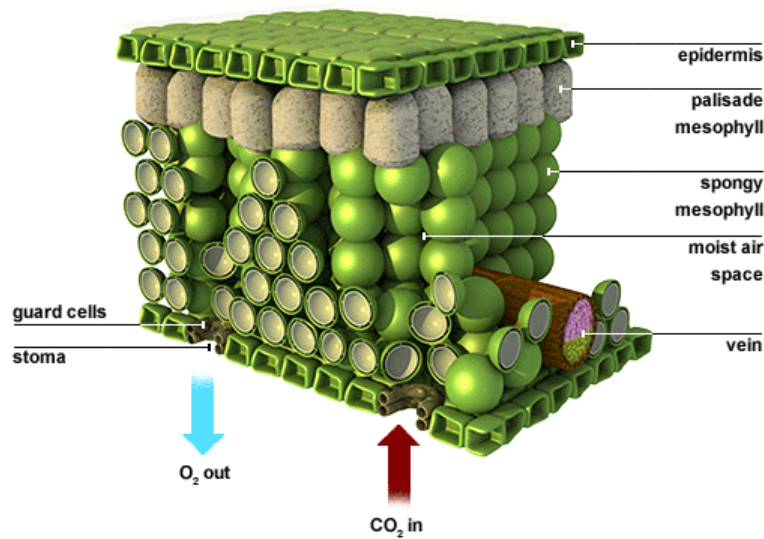


Figure 2.4: Internal structure of a plant [7].

content [53]. The near-infrared spectrum is a region where biochemical absorptions are limited to the compounds typically found in dry leaves, primarily cellulose and other structural carbohydrates [54]. In a typical green leaf, the near-infrared reflectance increases dramatically about 76%. The reasons that healthy plant canopies reflect so much near-infrared energy are basically two: the leaf already reflects 40 to 60% of incident near-infrared energy from spongy mesophyll, and the remaining 45 to 50% of the energy penetrates through the leaf and can be reflected once again by leaves below it. Because the photon energy at wavelengths longer than about 700 nanometers is not large enough to synthesize organic molecules. A strong absorption at these wavelengths would only result in overheating the plant and possibly damaging the tissues.

Infrared wavelengths reflected by plants are also important to determine plant stress. Rays of those wavelengths are likely to pass through many more interfaces of the leaf than the corresponding light rays of the visible wavelengths. As a consequence, near-infrared radiation gets through cell structure of the plant interacting with it and giving information about it [55]. When plants are actively photosynthesizing, they reflect or scatter near-infrared light. On the contrary, when photosynthesis has an abnormal

behavior, plants get stressed due to the absorption of near-infrared wavelengths. Near-infrared radiation causes overheating and tissue damage.

2.3.2 Vegetation curve and spectral bands of vegetation

There is a characteristic curve that concerns on vegetation's health. This curve is composed by reflectance values along visible and near-infrared spectra. Fig. 2.5 illustrate three reflectance curves for vegetation at different stages according to the health status. Analyzing Fig. 2.5, healthy and stressed vegetation absorb red radi-

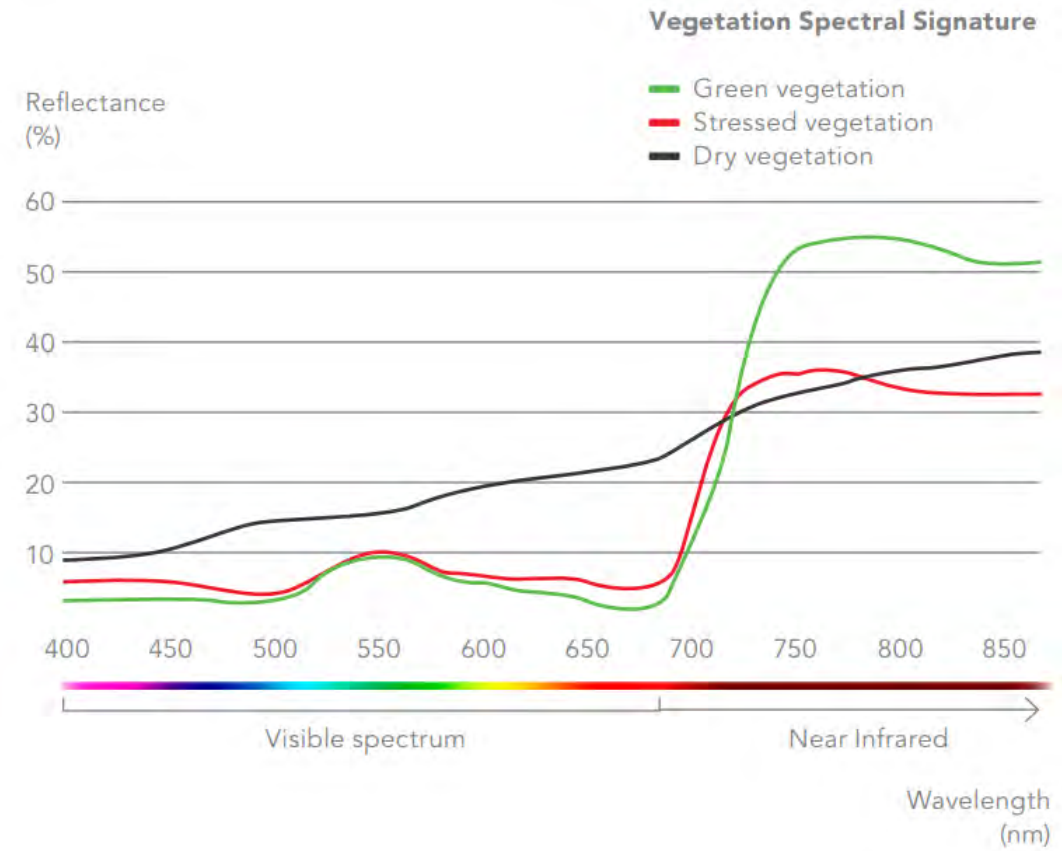


Figure 2.5: Reflectance curves for vegetation at different stages [8].

ation at similar rate. Near infra-red reflection drastically decreased from healthy to stressed vegetation. Stressed to dry vegetation increased drastically its reflectance in red wavelengths, while near-infrared reflection slightly decreases. Considering that, the

wavelengths that presents a notable change in reflectance values according to the health status of a plant are ranged from 600 to 800 nm. Green radiation can be used also to determine some features of vegetation but mostly red and near-infrared wavelengths are studied to identify plant diseases.

In the following subsections, information about the most relevant bands is addressed, mentioning their relationship with important vegetation features.

Green band

The green band corresponds to wavelengths between 500 and 600 nm. This band has the greatest reflectance of a plant in the visible spectrum. It is strongly associated with the amount of chlorophyll that a plant contains. As mentioned before, chlorophyll absorbs red and blue wavelengths but reflects green wavelengths mostly in summer when chlorophyll is at its maximum. On the other hand, in fall there is less chlorophyll in the leaves, so there is less absorption and proportionately more reflection of the red wavelengths, making the leaves appear red or yellow.

Red band

The red band is ranged between 600 and 700 nm of the visible spectrum. In this band exists the strongest chlorophyll absorption. For most crops this band gives an excellent contrast between the plants and the soil. It is extensively used for compiling most of the vegetation indices in agriculture.

Red edge band

This is a narrow band located between 700 and 740 nm approximately. As in Fig. 2.6, it is the point of sudden change in reflectance, from strong absorption of red radiation to substantial reflection of near infrared in healthy vegetation. This band is very sensitive to plant stress and it also provides information about the chlorophyll [14].

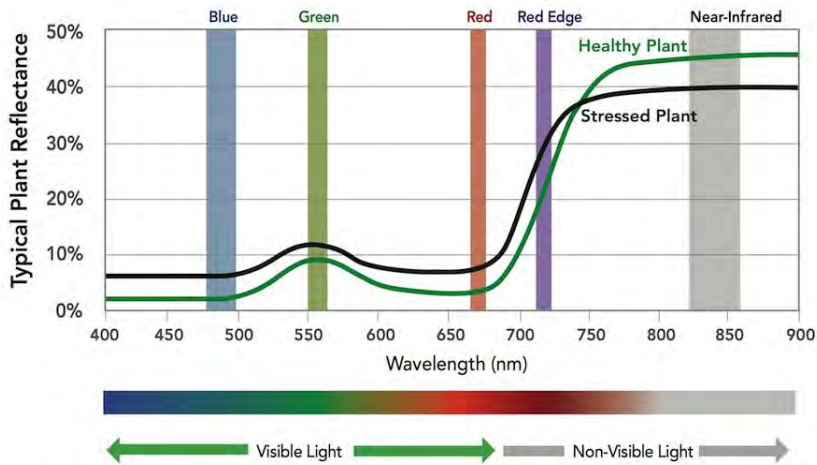


Figure 2.6: Reflectance curve of vegetation [8].

Near-infrared band

In larger wavelengths, there is located the near-infrared band. This band corresponds to wavelengths located from 770 to 2500 nm. This band has the strongest reflectance of the bands previously mentioned. A highly significant variation of the reflectance in this band is produced when a plant is under stress. Near-infrared reflection is also related to the chlorophyll content in a plant [56]. This portion of the electromagnetic spectrum provides critical data to monitor changes in crop health like moisture and stress analysis, water management and plant counting. A plant with more chlorophyll will reflect more near infrared energy than an unhealthy plant.

Short-wave infrared band (SWIR)

SWIR ranges from 0.9 to 1.7 μm . A large absorption by leaf water occurs in this spectrum and the reflectance from plants thereby is negatively related to leaf water content. An increased reflectance in these wavelengths is the most consistent leaf reflectance response to plant stress in general, including water stress [57]. This can be seen at Fig. 2.7.

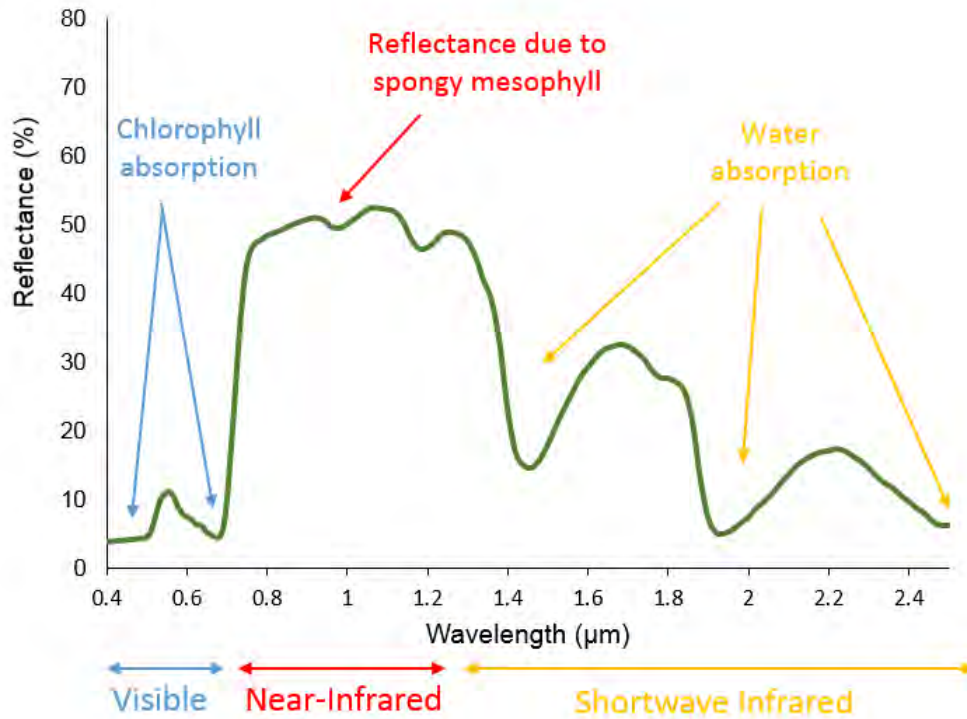


Figure 2.7: Extended reflectance curve of vegetation [9].

2.3.3 Vegetation indices

Information obtained from multiple spectral bands can be used to determine health status of the vegetation through image processing using specific algorithms. These algorithms are designed to provide the so-called vegetation indices, which commonly are the ratio between the functions of pixels values in different spectral bands. Vegetation indices can be defined as dimensionless, radiometric measures that work as indicators of relative abundance and activity of green vegetation.

An image containing vegetation can be processed in order to obtain a specific vegetation index. The spectral information needed may be extracted from the pixel value of the required band. Then, the value will be used as input into the vegetation index function. This process is applied to every pixel in an image. As a result, a new image containing a vegetation index value for each pixel will be obtained. The range of the

values of the image would vary according to the index.

There are many vegetation indices that determine certain vegetation characteristic that is being monitored like water stress or chlorophyll level. They also may vary according to the spectral bands that are required to compute the index. Some use visible spectrum bands like the Normalized Difference Vegetation Index (NDVI) and Normalized Difference Red Edge(NDRE) index that uses red edge and red bands. Others require from near-infrared to short-wave infrared radiation to compute the index the Crop Water Stress (CWS) that requires two specific bands in the thermal range.

2.3.4 Normalized Difference Vegetation Index

A popular vegetation index that allows to identify and quantify vegetation health is the *Normalized Difference Vegetation Index* (NDVI). This index is obtained by computing the ratio between the subtraction and the sum of near-infrared radiation and red radiation reflected by a plant as follows

$$NDVI = \frac{\rho_{NIR} - \rho_R}{\rho_{NIR} + \rho_R} \quad (2.31)$$

where ρ_{NIR} corresponds to the near-infrared reflectance value of the pixel and ρ_R corresponds to the red reflectance value of the pixel. The red pixel value may be obtained from the red band of the visible reflectance image.

NDVI is ranged from 1 to -1. As previously mentioned in the last subsection, healthy vegetation absorbs most of visible light but the reflectance of the infrared tends to rise dramatically. According to (2.31), the previous conditions will lead to a NDVI value close to 1. Unhealthy vegetation reflects the majority of visible light spectrum but near-infrared reflection will decrease. Analyzing (2.31) again, with these new conditions, NDVI values close to 0 will be obtained.

We may say that having low NDVI values is translated into a low chlorophyll concentration, which is an indicator of infestation, bad nutrition or lack of water. Having high NDVI values means that the vegetation is healthy.

In order to obtain the corresponding NDVI values from a certain region, we have to perform certain image computations from the pixel values of the corresponding aerial imagery. For that, it is required to have a pair of images:

- a) a near-infrared reflectance image;
- b) visible reflectance image.

After the image processing of the two images, the NDVI can be computed.

CHAPTER 3

Methodology

Alternatively to the use of commercial multispectral sensing devices, in this work a low-cost alternative system has been developed in order to obtain similar multispectral imagery with the use of standard digital cameras. The use of such cameras have some cons with respect to the use of commercial ones. These disadvantages are listed next. Some digital cameras can only be triggered mechanically with an external button making the trigger task hard to handle during flights. Another limitation is that the storage of a picture in the external memory of the cameras is not fast using its native firmware. Finally, unlike specialized multispectral sensors, digital cameras lack of an automatic georeference system.

In this chapter, the methodology developed to achieve the main objective of the project is explained. The content is divided in many subsections related to the equipment, devices and software used as well as all the steps involved in this process.

3.1 System description

The main contribution of this work is the implementation of a low-cost and easy-to-implement Unmanned Aerial System able to collect multispectral imagery for crop monitoring. Such system is composed of hardware and software parts. The complete system will be responsible for: a) acquiring the images from a predefined crop field or a desired area; b) processing the images into orthomosaics that will be used to compute the NDVI of the selected region. For that, an UAV is constructed and equipped with a two-camera rig, autopilot, external sensors and a microcomputer. All these parts are connected as Fig. 3.1 shows.

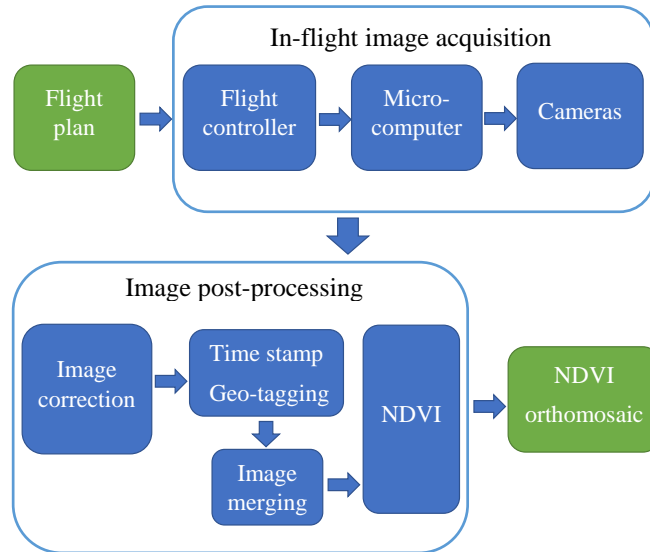


Figure 3.1: The overall aerial imaging system architecture.

As shown in Fig. 3.1, the complete system is divided in two main processes. The first section is related to the in-flight image acquisition and is composed by the implementation of the imaging system on the UAV. The second section corresponds to the image processing of the aerial imagery which involves the use of software implemented off-line.

3.1.1 Hardware components

The quad-rotor used in this system as well as all its parts are shown in Fig. 3.2. It is basically composed of a flight controller and a set of sensors and communication devices, a set of motors, drivers and propellers, a battery, a microcomputer and a camera rig composed of two digital cameras. The quad-rotor is equipped with a radio receiver to

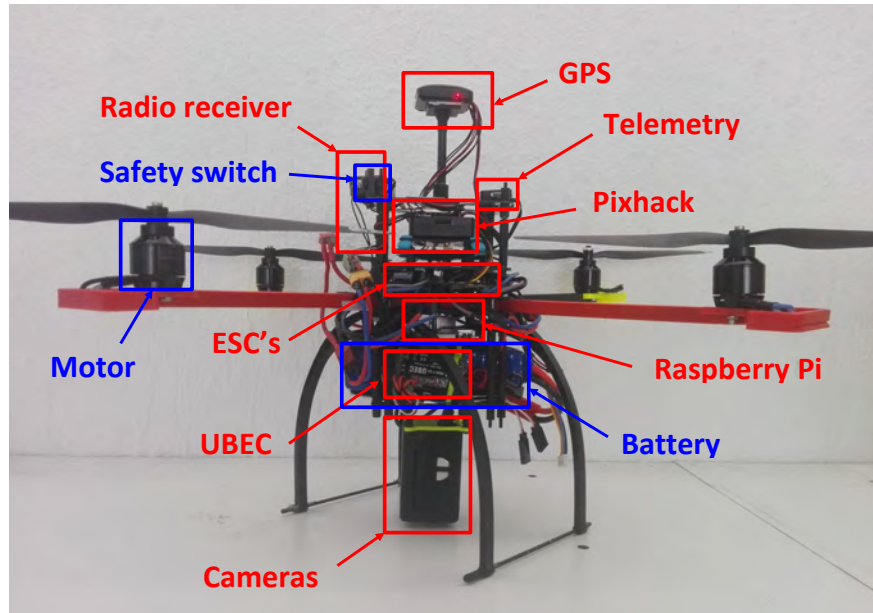


Figure 3.2: Quad-rotor components equipped with the imaging system.

receive commands from a radio control. A 433 MHz telemetry is also equipped in the drone to receive information from the sensors and flight into the visual interface at the ground station. The microcomputer mounted in the drone is a Raspberry Pi. To power the microcomputer a 5v Universal Battery Eliminator Circuit (UBEC) is used. To arm the vehicle there is a safety switch located at the top of the frame as shown at Fig. 3.2. The specifications of the quad-rotor are listed in Table 3.1.

The CUAV Pixhack autopilot was used over the Pixhawk due to some improvements. In this device, the IMU has been isolated from vibrations. The IMU sensors are mounted in a floating platform to ensure most accurate sensor readings. In addition the IMU platform features a large anti-interference shield which ensures the sensors will not

| Parameter | Value |
|-----------------------|---|
| Span | 50 [cm] |
| Height | 24 [cm] |
| Weight | 1.4 [kg] |
| Propulsion | Brushless motor 760 [kv] Propeller 10x4.5 [in] |
| Max. Load | 3.3 [kg] |
| Battery type | Li-Po 4s Capacity 5000 [mAh] |
| Flight controller | Pixhack v3 |
| Firmware | ArduCopter 3.5.5 |
| Estimated flight time | 15 [min] |

Table 3.1: Quad-rotor parameters.

report false values [58].

Due to the low cost and light-weight, two Mobius ActionCam cameras were chosen to collect the multispectral imagery needed. The specifications of the camera are shown in Table 3.2. These cameras were located at the bottom of the UAV just below the

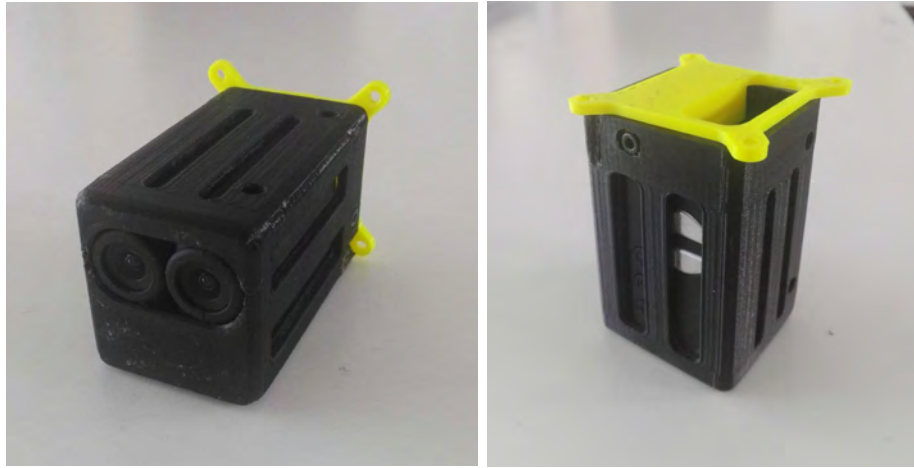
| Mobius ActionCam | |
|------------------|----------------------|
| Parameter | Value |
| Focal length | 2.1 [mm] |
| Image size | 2304 × 1536 [pixels] |
| Sensor size | 5.07 × 3.38 [mm] |
| Horizontal FOV | 60° |
| Vertical FOV | 90° |
| Weight | 38 [gr] |

Table 3.2: Camera parameters.

battery as can be seen in Fig. 3.2. To attach the cameras to the quad-rotor frame a 3D printed mounting structure was designed as seen in Fig. 3.3.

3.1.2 Software components

Part of the software used in the system is based on open-source software available on the Internet. However, certain specialized software has been developed by the authors.



(a) Frontal view.

(b) Side view.

Figure 3.3: Cameras mounting rig developed in the LAB.

The firmware used for the flight controller is ArduCopter 3.5.5 developed by ArduPilot. This platform is widely used to control UAS. A compatible ground control interface is also available to use along ArduPilot platform [59]. This interface is Mission Planner. Mission Planner is a graphic interface that allows the user to visualize the parameters of the UAV, i.e., attitude, heading and GPS status. It also allows to configure parameters of the flight controller and plan flight trajectories. An image of the interface is shown in Fig. 3.4. OpenDroneMap (ODM) is an open-source software used to merge the aerial imagery into orthomosaics. This software is able to generate 2D and 3D models from a set of aerial imagery [60]. Another open-source software used is Fiji which is an image processing package [61] that contains several plug-ins useful for scientific image analysis; the plug-in used to compute the NDVI is named *Photo Monitoring*. The script executed by the Raspberry Pi and the scripts dedicated to do part of the image post-processing were implemented in Python with the use of OpenCV libraries. All these scripts were developed by the authors.

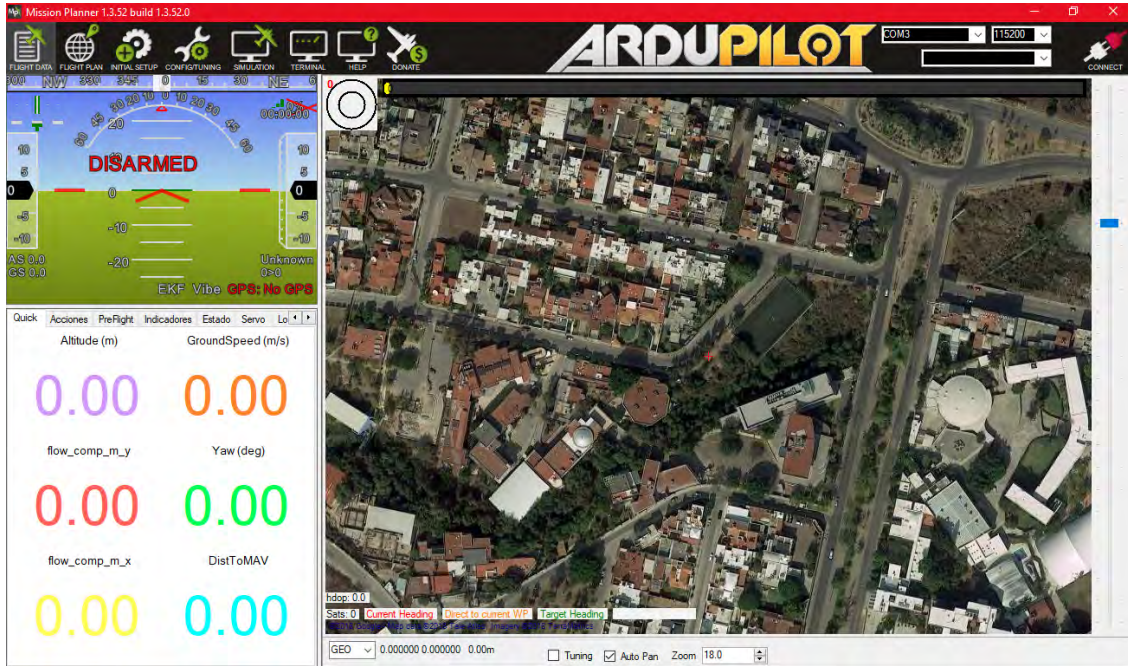


Figure 3.4: Mission Planner.

3.2 Multispectral camera design

To compute the NDVI, it is necessary to obtain red and near-infrared reflectance values from the vegetation. For this purpose, we have used the two digital cameras already mentioned. One camera will be used to capture visible spectrum, specifically the red radiation. This camera will be kept unmodified. The other camera will be used to capture near-infrared spectrum. To achieve this, the camera will suffer some modifications in order to make it sensitive to near-infrared radiation.

A standard camera captures wavelengths from 400 to 700 nm approximately. This is due to an internal IR cut filter that blocks any wavelength longer than 700 nm. Figure 3.5 illustrate the quantum efficiency of the color sensor that the Mobius cameras use. This plot shows the quantum efficiency for each color according to the Bayer filter in the Aptina sensor.

According to the quantum efficiency of the sensor, in Fig. 3.5, the three color bands are sensitive to near-infrared wavelengths that correspond beyond the 700 nm. The red

Quantum Efficiency – Color Sensor

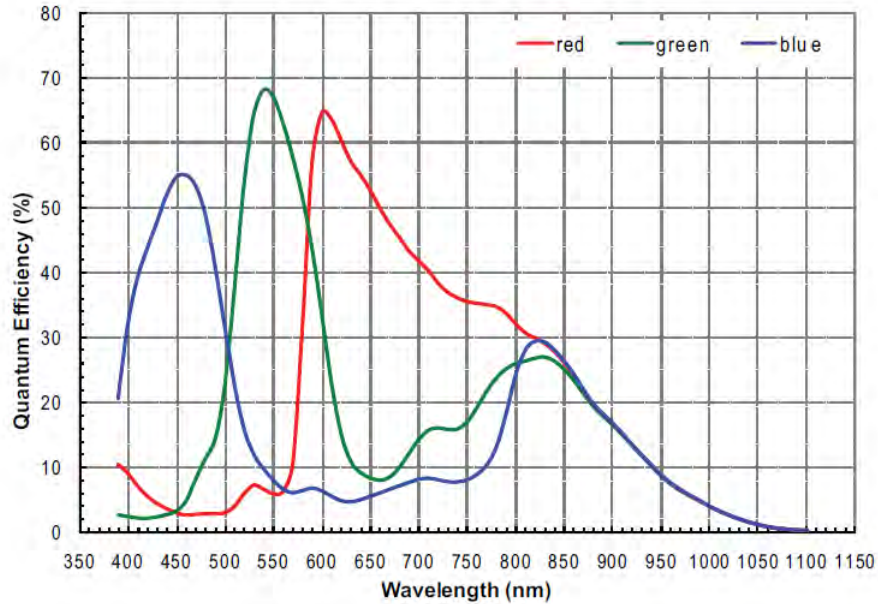


Figure 3.5: Quantum efficiency of the Aptina sensor.

band is the most sensitive to near-infrared radiation so it will be convenient to use this band to acquire this radiation. The only problem is that the camera also contain an IR cut filter that prevent this radiation to pass into the sensor. Removing this filter allows the camera to capture wavelengths from the previous limit of 700 to 1100 nm which is the range of near-infrared spectrum [28]. Additionally, a red filter can be added to block wavelengths shorter than 600 nm approximately. Fig. 3.6 shows the transmission curve of a Wratten 25 gelatin filter or commonly called red 25 filter. This filter will help to block radiations shorter than 600 nm to be sensed by the camera.

With the mentioned modifications, the camera is allowed to capture red to near-infrared wavelengths. The red band of a modified camera with this method has been proved to be more sensitive to infrared radiation [37]. As infrared radiation can be obtained from that band, this reflectance value can be used along red reflectance from the unmodified camera in 2.31 to obtain the NDVI.

Another filters used are the Wratten 15 and Wratten 25A. The first filter blocks blue wavelengths letting pass green, red and near-infrared light. Blocking the blue

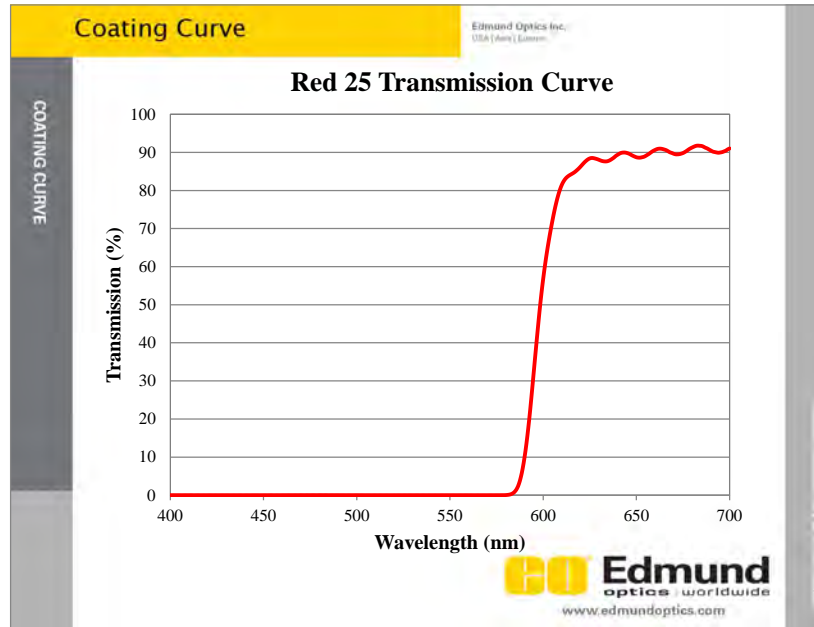


Figure 3.6: Wratten 25 transmission curve.

channel allows the camera to capture mostly near infrared light. This modification also allows the red channel to capture a mix of red and near infrared. There is a difference between these two filters. The Wratten 25A absorbs wavelengths shorter than 580 nm approximately so the green is blocked and the light captured in this channel is mostly near infrared similarly to wratten 25. Green light is not needed to compute the NDVI so, using any of the previous filters is a viable option for multispectral imaging because it allows to capture more near infrared spectrum in the bands related to blue and green which are not being used.

3.3 Flight trajectory

In order to obtain aerial imagery using an UAV, the first step is to establish a trajectory that the vehicle will follow according to the area of interest. For the trajectory we have used Mission Planner. Mission Planner is a ground control station interface compatible with the ArduPilot platform. This software can be connected to any flight controller based on Pixhawk flight autopilot.

Trajectories can be done using manual flight modes. The most common manual modes are mentioned next. *STABILIZE* mode allows the user to manipulate the vehicle with the radio control. *LOITER* mode allows the user to maintain the UAV at a fixed altitude and fixed position if not any input from the radio is received. Finally, *ALT-HOLD* mode allows the user to maintain the UAV fixed at a specified altitude. Trajectories can also be planned manually using way points at specific locations. These points will guide the UAV. Another way to elaborate flights trajectories is using polygon points which will automatically generate a flight trajectory according a selected area. These kind of trajectories are performed only in *AUTO* mode. This mode automatically executes the flight commands specified in a planned flight trajectory. Once the final trajectory has been created, it can be uploaded to the UAV for a later execution.

The flight trajectory used in this procedure will be planned according to the use of polygon points around the area that is going to be covered. The default trajectory generated by Mission Planner using polygon points is a grid. This grid is composed by flight trips along the selected area.

3.3.1 Photogrammetric Parameters

Post-processed aerial imagery is intended to be merged into an orthomosaic with OpenDroneMap which is a software that assembles multiple images into an orthomosaic. If images are not good enough, the merging process will fail or will result in a bad quality orthomosaic.

Flight trajectory requires to consider some requirements related to basic photogrammetric parameters in order to obtain an acceptable imagery. These photogrammetric parameters are the overlaps which will give information about how much distance should exist between the capture of the images along the trajectory planned and between flight trips. A flight trip is a linear trajectory included in the flight plan.

There are two kind of overlaps: side laps and end laps. These overlaps exist between and along flight trips, respectively. Overlaps are shown at Fig. 3.7.

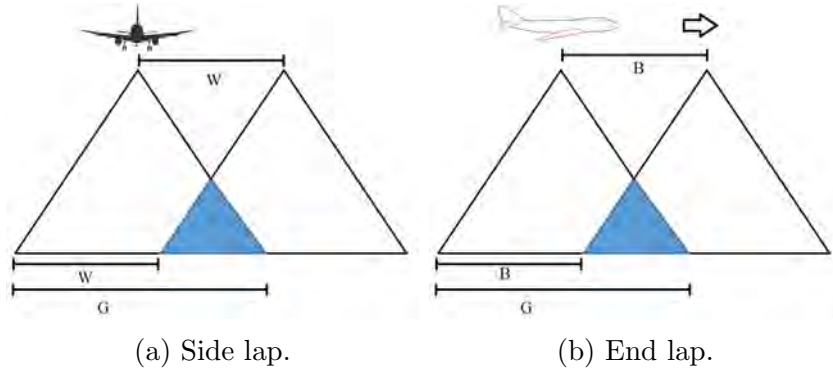


Figure 3.7: Graphic representation of overlaps.

End lap can be calculated using (3.1) and is expressed as a percentage as follows

$$PE = \frac{G - B}{G} \times 100 \quad (3.1)$$

where G is the dimension of the ground covered by an image and B is the distance between image captures. In order to prevent gaps in an orthomosaic due to crab, tilt, flying height and terrain variations, a normal value for end laps should be about 60%, with a tolerance about 5% [62]. On the other hand, **side lap** is calculated using (3.2).

$$PS = \frac{G - W}{G} \times 100 \quad (3.2)$$

where G is defined as in (3.1) and W is defined as the distance between trigger points. Side lap is normally set to 30% to avoid gaps in orthomosaics caused by drift, crab and tilt [62].

Values ranging from 70% to 75% of end lap, and 60% to 80% of side lap are commonly used in applications related to aerial photogrammetry [31], [26], [41].

The generated trajectory can be modified by changing flight height and overlaps. The distance between the trigger event changes as the end lap is increased or decreased. This distance corresponds to B which is illustrated in Fig. 3.7b.

3.3.2 Camera Trigger System

Using the flight plan tool of Mission Planner, photogrammetric flights can be designed with customized trigger points. There are two ways to control a camera using a customized flight plan. The first one is setting way point as trigger point. This means that when the vehicle is flying over that point, a trigger signal from the flight controller will be activated. The second way to do this is enabling a command at certain way point. This command is called *DO_CAM_TRIGG_DIST* and its function is to set a distance in meters that need to pass to activate the trigger signal. This action will be active while the command is enable and will stop when the command is set to a value of 0 m.

The camera trigger can be activated by the flight controller through a trigger event that can be linked to one of its auxiliary outputs. So every time that the trigger event is active the selected auxiliary output will conduct a high logical value. This signal will have a customized duration that can be configured in Mission Planner.

As mentioned before, there is not a method to link trigger signal from the flight controller with the Mobius cameras. Instead, the use of an embedded microcomputer will help controlling the trigger of the cameras via software. The on-board computer must detect the trigger event commanded by the flight controller and then, manipulate the cameras to take a picture. When the trigger event is active, the digital signal from the auxiliary output will be detected by a python script inside the Raspberry Pi. This script will be able to control the cameras using the VideoCapture module from OpenCV. As first step, the cameras will be initialized, then some parameters of the cameras will be configured. As next step, the script will maintain the cameras active so when a trigger signal is recognized a video frame from both cameras can be captured and saved as images inside the on-board computer memory. Images from both cameras are stored in two folders related to visible and near-infrared images. This system is shown at Fig. 3.8.

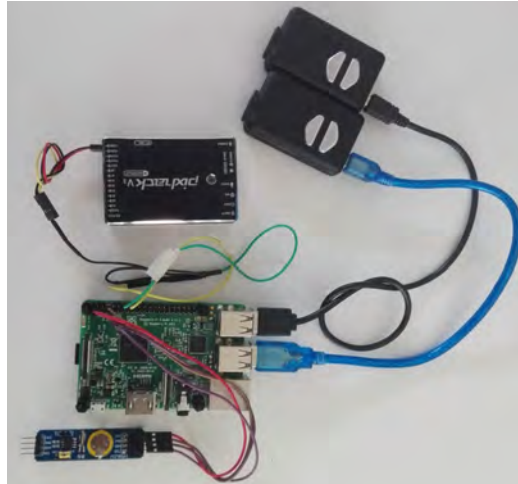


Figure 3.8: Elements that integrate the trigger system : flight controller, microcomputer and cameras.

3.4 Image post-processing

3.4.1 Georeferencing

In order to generate orthomosaics from the aerial imagery of both cameras, it is necessary to georeference all the images with the position where each image was taken. This task consists in adding *latitude*, *longitude* and *altitude* information to specific tags inside the metadata of an image. Locating the image at a specific position and altitude where the image was taken is useful for reconstruction algorithms that generate orthomosaics. The cameras used do not georeference the images taken. Mission Planner has a georeferencing tool that can be used to solve that problem. This tool take GPS coordinates from specific data stored in the log file of each flight. This data correspond to the *CAM* messages. A *CAM* message is a type of structure that contains time, latitude, longitude and altitude values related to a trigger point where a images are taken. To add these data to the images, a correct matching of the *CAM* messages should be made with the images. So, the first requirement is that the number of *CAM* messages should be the same as the selected images. To do this, a log file of a specific flight and a folder of images should be selected in the georeferencing tool. The match

is done by comparing time between images and *CAM* messages so, it is required that such images contain a timestamp in their tag related to the time of capture.

3.4.2 Orthomosaic generation

Having an orthomosaic of the shot area is useful because having a single image will help to analyze it easily rather than analyzing the whole set of images. An orthomosaic is a composite image based in the 2D reconstruction of certain area using aerial imagery. The reconstruction is done by image processing algorithms involving matching of characteristic points and geolocalization data contained in the metadata of an image. Some softwares allow to generate 3D models of the surface by creating cloud points of the images given. This models are useful for mapping applications. Final orthomosaics are commonly represented in TIFF formats. These kind of image formats are multilayer images that contain extra data compared to a simple JPG images.

Most of georeferencing softwares require georeferenced JPG images to achieve an adequate matching and resizing of images, which are needed to assemble them into an orthomosaic. To begin the matching and alignment process of the images, OpenDroneMap requires a set of images that may vary according to the performed flight. Once the images are uploaded to the software, a set of parameters related to the matching process can be configured to achieve a good image processing. These parameters may be changed according to previous failures in the orthomosaic generation, allowing the improvement of the process on new tries. When the process is finished, ODM allows the user to download the resulting image as PNG and TIFF format of the 2D reconstruction. The 3D model can be downloaded as cloud points.

3.4.3 NDVI computation

NDVI will be computed taking the near-infrared and visible orthomosaics generated by OpenDroneMap. The Photo Monitoring plug-in of Fiji software works only with JPG images so the PNG images will be converted to JPG to process them and compute the

NDVI. Additionally, Fiji requires the images to contain same timestamp related to the time of capture. To overcome this issue, a simple metadata insertion script, similar to the one used to insert time to the images taken, will be used to insert an arbitrary time. Both JPG orthomosaics, visible and near-infrared must contain the same timestamp. Once the images are ready to be processed by the plug-in, these images are selected to start the NDVI computation. The NDVI is computed by the software as in (2.31). ρ_{nir} and ρ_{red} now correspond to the pixel values of the red bands in the near-infrared and visible images, respectively.

CHAPTER 4

Experiments

In this chapter it is shown and discussed the results of the system tested under predetermined conditions. A video of the conducted experiments can be seen at https://drive.google.com/file/d/1xxWdcDsGksYrpAzBeY92pzigGW7o_67u6/view?usp=sharing

The chapter is divided into general sections related to the fundamental steps of the developed methodology .

4.1 Camera testing

Following the methodology exposed in the previous chapter, certain modifications were required to be done to one of the Mobius Cameras in order to make it sensitive to near-infrared wavelengths. First change is to remove the internal IR cutoff filter that blocks infrared radiation to be sensed by the internal sensor. Then, a Wratten 25 gelatin filter should be added. According to Figure 3.6, this filter blocks any radiation shorter than 600 nm, so the spectrum captured by the camera ranges from red to near-infrared

radiation.

Lenses of both cameras are shown in Fig. 4.1. The IR cutoff filter of the unmodified lens can be appreciated due to the magenta color. Red filter can be seen in the lens of Fig.4.1b.



(a) Unmodified lens.



(b) Modified lens.

Figure 4.1: Lenses of both cameras.

Mobius cameras may be equipped with a micro SD memory where firmware and settings are stored. In this modality, the cameras can be used manually to capture images or video. Although the firmware limits the capability of taking pictures at specific time, it allows to configure several parameters. In order to acquired images when required, the SD card must be removed from the device so it can be triggered via software with a python script.

A module from OpenCV called VideoCapture was used to control the cameras [63]. This manipulation involved the configuration, initialization and storage of images. VideoCapture allows to perform some actions on the camera by USB interface of both devices connected to the on-board computer. With this module, maximum resolution of images was found to be 1280×720 pixels, even though the camera is able to capture at bigger resolution. So, via software, the camera can not be set with a higher resolution. According to Table 3.2, the maximum resolution of the cameras using their native firmware is almost the twice the one selected with OpenCV. This is a problem that can be resolved in a future work, however it does not affect the results, only the

image resolution.

The script that store images taken with the camera does it every time that the trigger signal is detected by the Raspberry. This signal comes from the flight controller when the trigger event is active within a flight plan or due to a manual trigger. Manual trigger can be done linking the trigger event to a specific channel from the radio control. To test the trigger system, the trigger event was linked to channel 7 of the radio control which corresponds to a switch. Every time that the switch is activated, a trigger signal must be send to the microcomputer allowing the capture of an image.

To acquire the first aerial images, the imaging system was attached to the quad-rotor. The vehicle was placed over an area of vegetation in *LOITER* mode. Being placed at that fixed position, a pair of images were taken. The image taken with the unmodified camera has been split into their individual bands: red, green and blue. These images are shown in Fig. 4.2.

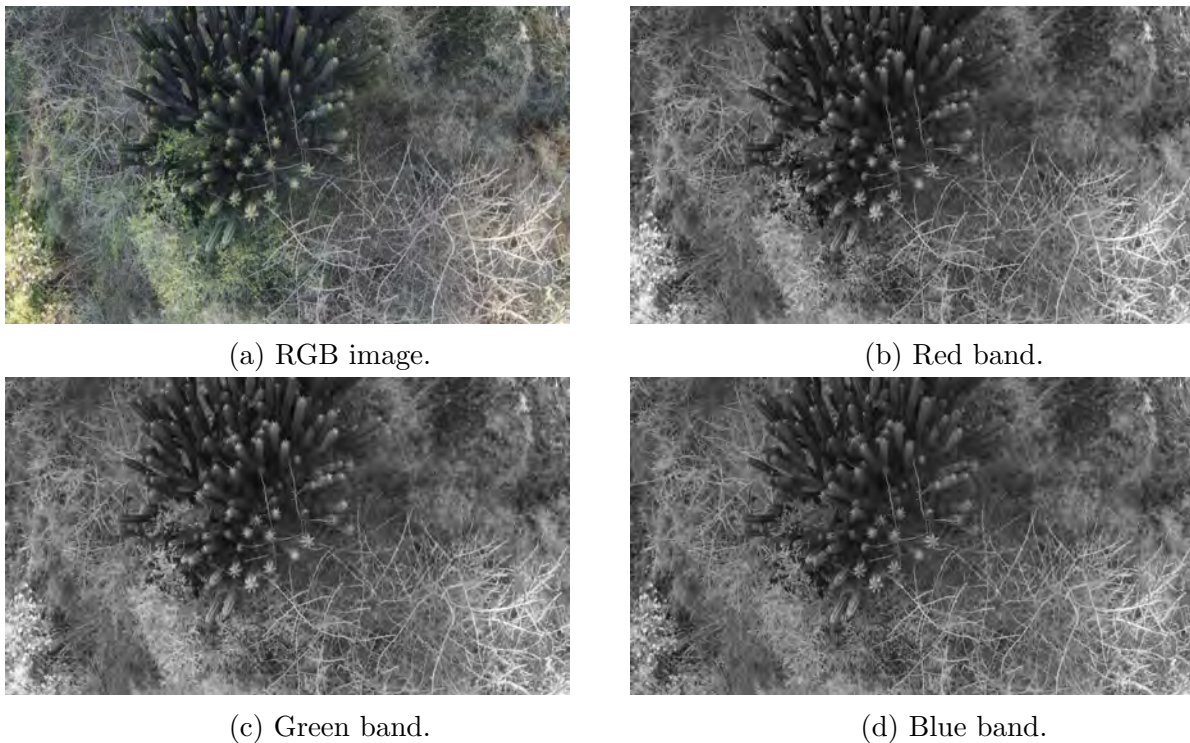


Figure 4.2: RGB image split into individual bands.

Same area was captured with the modified camera in another image. This image

is intended to capture the near-infrared radiation. The image of the area is shown in Fig.4.3a. This image has reddish hues, this is due to the red filter added so, blue and green colors are not present in the image.

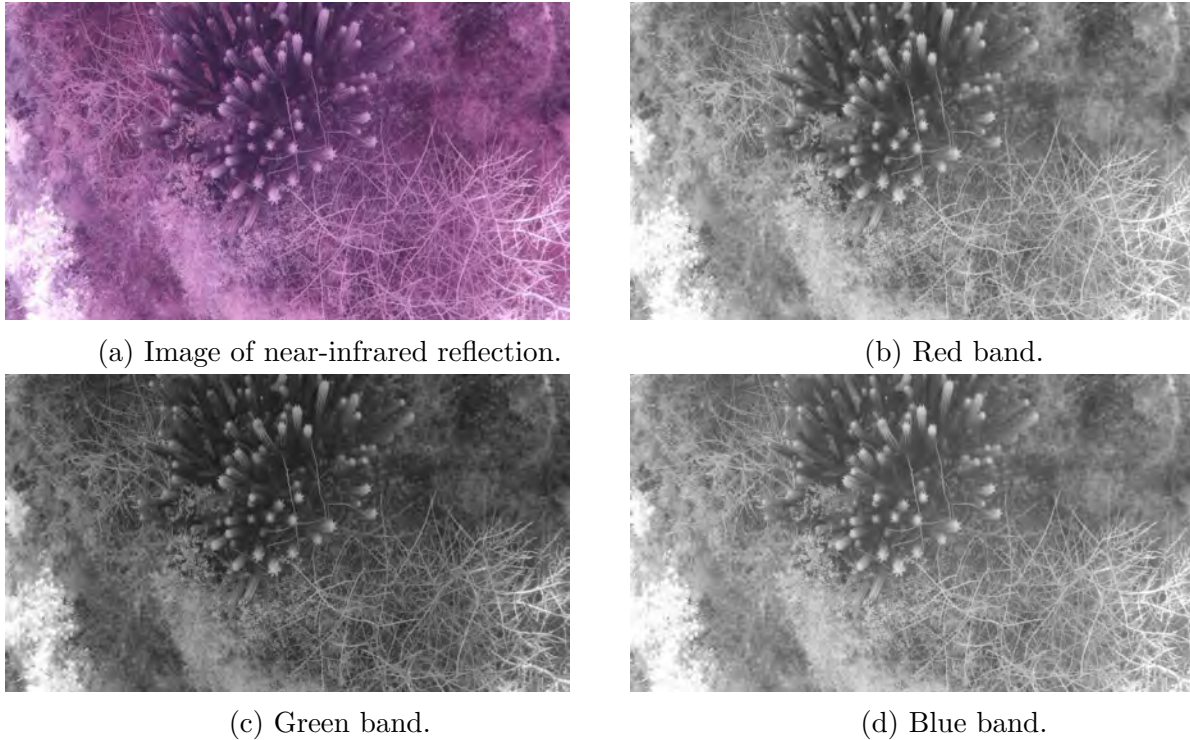


Figure 4.3: Near-infrared image split into the individual bands.

The image was also split into their individual bands as in Fig.4.3. The three bands are sensitive to near-infrared, being the red band the most sensitive. This is due to the quantum efficiency of the camera shown in Fig. 3.5. This fact can also be sustained seeing that in Fig. 4.4 red band contains a slightly larger concentration of the highest values of intensity. As conclusion, red band allows to capture with high efficiency from red edge to near-infrared. After this analysis, the red band of the modified camera will be selected to be used as input in the NDVI computation.

To verify that the NDVI could be computed using the images obtained from both cameras, a first test was made introducing a pair of images to the NDVI algorithm of the Photo Monitoring plug-in. The images used for this were the ones shown in Fig.4.2a and Fig.4.8a. The image obtained is shown in Fig.4.5a

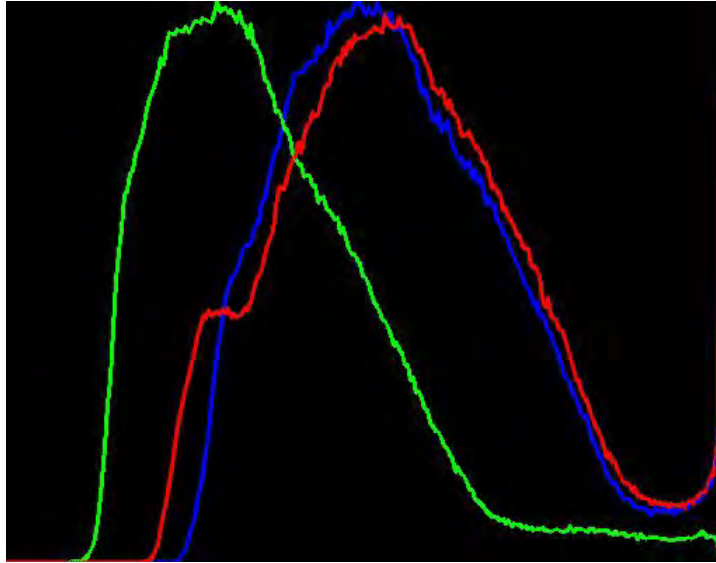
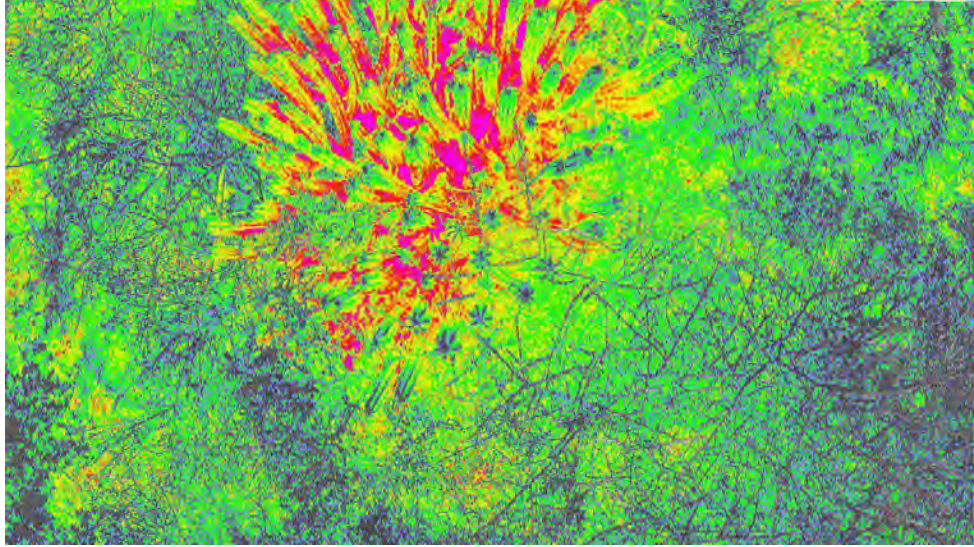


Figure 4.4: Histogram of the three bands of a near-infrared reflectance image. Horizontal axis represents pixel values (0 - 255) and vertical axis represents frequency of values.

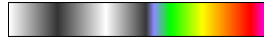
What Fiji does, is that point features are extracted from both images and then, a matching process between both images is done. Once this is done, a crop is applied to both images to obtain images of same size. Then, NDVI is computed using those images. It can be seen in Fig.4.5a a large area corresponding to shadows that appear in magenta. According to the color map in Fig.4.5b, this is the maximum value that can be obtained. This is due the lack of intensities in the red band of the unmodified image. So, with values close to zero for red radiation in (2.31), a value close to 1 is obtained in the NDVI. Besides this issue, the upper surrounding vegetation is detected as it takes intermediate values between 0 and 1, being the yellow and red colors the representation of healthy vegetation. With gray shades is represented the dry vegetation.

4.2 Photogrammetric parameters and flight plan

To test the imaging system under the commands of a flight plan, it was necessary to attach it to the quad-rotor and perform a flight trajectory. This trajectory was generated using the flight plan tool of Mission Planner. The path generated by the



(a) NDVI image.



(b) Colormap.

Figure 4.5: NDVI computed with Fiji.

software was composed by flight trips along the covered area by the polygon tool of Mission Planner. This path contained default parameters of overlaps and height that were modified values used in similar applications mentioned in the previous section. In this case, end lap and side lap values intended to use were 85% and 75%. These values will provide good aerial imagery useful for ODM to make a correct matching. The height of the flight was set to 7 m. After setting these parameters, the trajectory was generated over the selected area as shown in Fig. 4.6. The area corresponds to a soccer field covered with artificial grass.

Within the trajectory, red marks are the polygon points that bound the area of interest. Inside this area, there are green points that will guide the vehicle along the generated path. These points correspond to take-off, land, and trigger events. It is also marked the home location. One of the output data was the distance between images B . This was computed by Mission Planner with a value of 2 m. To verify the accuracy of this value, the end lap and side lap values can be used to determine B in (3.1). Therefore, from (3.1), B can be computed. But first, G must be known. Using some

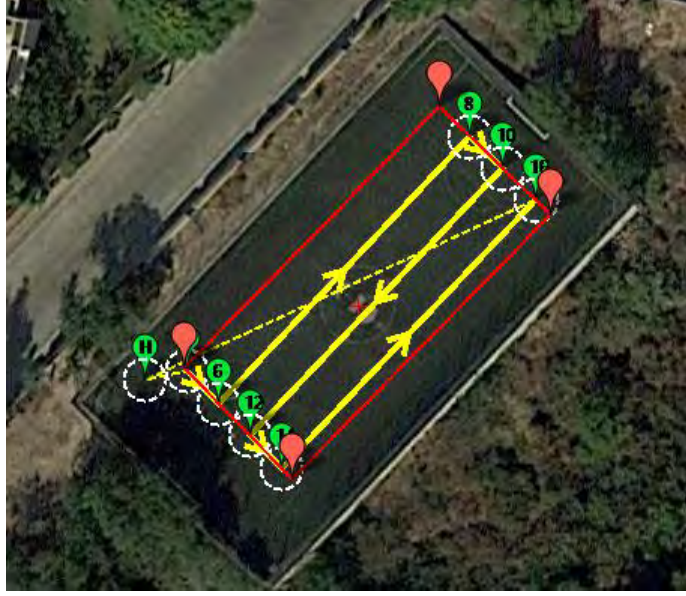


Figure 4.6: Flight trajectory generated by Mission Planner.

trigonometry to the triangle of Fig. 3.7b, G can be computed as follows:

$$G = 2 \times H \times \tan \frac{FOV}{2} \quad (4.1)$$

where the Field of view (FOV) related to this side of the camera is 90° , implying that 45° must be used in (4.1). It follows that:

$$G = 2 \times 7 \text{ m} \times \tan 45^\circ = 14 \text{ m} \quad (4.2)$$

Then B can be determined solving (3.1) for this value, which leads to (4.3):

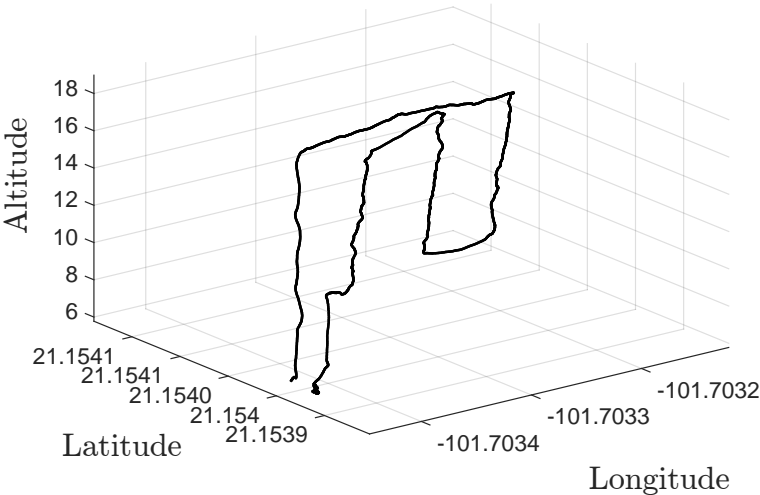
$$B = G - \frac{G \times PE}{100} \quad (4.3)$$

Using the mentioned overlap B can be calculated as:

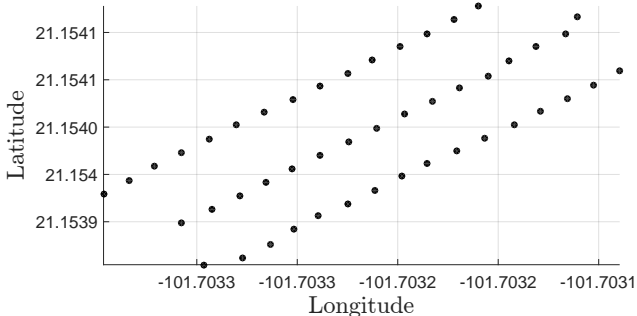
$$B = 14 \text{ m} - \frac{14 \text{ m} \times 85}{100} = 2.1 \text{ m} \quad (4.4)$$

So 2.1 m is the distance that must exist before shoots. It can be seen that both values of

B are very close. Note that flight plan generated by Mission Planner must be programmed with these values of overlaps.



(a) Trajectory performed by the UAV according to the flight plan.



(b) Location data from *CAM* messages.

Figure 4.7: Quad-rotor trajectory followed and points in space where the images are captured.

To command the trigger of the camera by the flight controller, the trigger event needs to be enabled according to a traveled value of B during the flight. The path generated by Mission Planner included several commands as mentioned previously. One of these actions is the command that enables the trigger event. There are two commands for this purpose: *DO_SET_CAM_TRIGG_DIST* and *DO_DIGICAM_CONTROL*. The first one is the command that is used in the project. This is able to generate a trigger signal

at regular intervals every time that a selected distance is traveled by the drone. The command is called first to set the parameter to the desired distance between shoots. It can be changed along the mission by calling again with a different value. At the end of the mission, it is called again to set the parameter back to zero which will stop capturing images. Using this command based on distance, results accurate enough as long as the GPS is giving good measures. Controlled by this command, the trigger signal comes out from one auxiliary output of the flight controller and goes to one digital input in the Raspberry. Once the script running in the on-board computer detected this signal, images from both cameras would be stored at that moment. The script is also able to store the capture time of each image. This is needed later in a step of the image post-processing.

After the flight over the selected area, a total of 47 images were stored in the on-board computer. These images are related to 47 *CAM* messages that were generated and stored in the log file of the flight. This information proves that the trigger subsystem worked perfectly acting every time that the flight controller enables the trigger event. *CAM* messages contain GPS position data where trigger events were active. As these messages are composed by coordinates, these data can be plotted to visualize specifically the section of the flight where the images were taken. The final 3D path followed by the drone according to the modifications in the flight plan is shown at Fig. 4.7a. In Fig. 4.7b it is shown the trigger points along the flight plan. It can be seen that the distance along the flight trajectory remained constant.

4.3 Image post-processing

4.3.1 Image rectification

From one of the initial flight tests, an aerial image of the same scenario was taken with both cameras as shown in Fig. 4.8a and Fig. 4.8b.

As a consequence of the lens type of the cameras, it can be seen that fish eye distortion

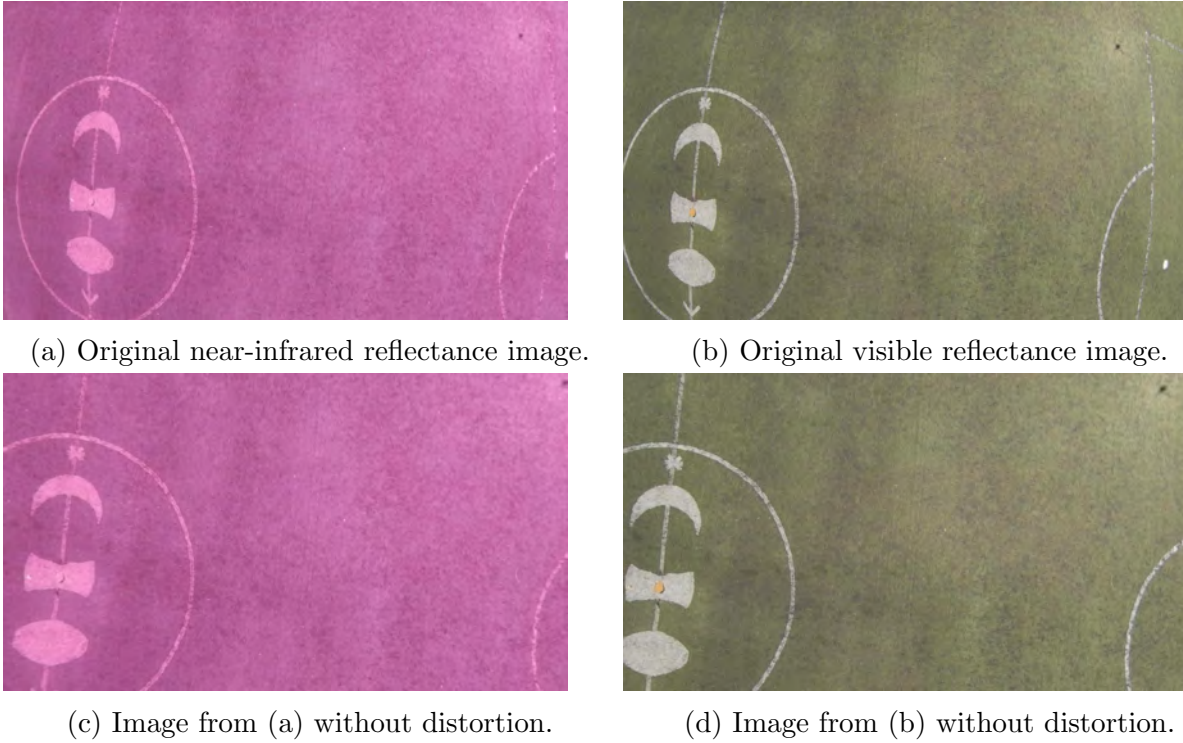


Figure 4.8: Images taken by the drone.

affected both images. This effect would affect the appearance of each orthomosaic if is not removed. So, a Python script was developed to remove this distortion of all the images. The rectified version of the original images are shown in Fig.4.8c and Fig. 4.8d. It can be seen, in the new image, that after the distortion removal size is lost due to a crop effect of the function that removes the distortion. The rectification process is done using the *undistort* function of OpenCV and is explained next. This function transforms an image to compensate for lens distortion. The camera matrix is needed for this process, such matrix contains the distortion coefficients and the camera intrinsic parameters. All this data can be used to rectify all raw images [64]. The camera matrix is shown next:

$$M = \begin{bmatrix} f_x & 0 & c_x \\ 0 & f_y & c_y \\ 0 & 0 & 1 \end{bmatrix}$$

where f_x and f_y are the focal length for x and y axes respectively. The optical centers

of both axes are represented by c_x and c_y . All these values are expressed in pixels. Distortion coefficients are related to the radial and tangential factor correction as:

$$x_c = x(1 + k_1r^2 + k_2r^4 + k_3r^6) \quad (4.5a)$$

$$y_c = y(1 + k_1r^2 + k_2r^4 + k_3r^6) \quad (4.5b)$$

$$x_c = x + [2p_1xy + p_2(r^2 + 2x^2)] \quad (4.6a)$$

$$y_c = y + [p_1(r^2 + 2y^2) + 2p_2xy] \quad (4.6b)$$

where the x_c and y_c correspond to the pixel position of the corrected image according to a x and y position in the distorted image. Here the subscript c means *corrected*; r refers to $r = \sqrt{x^2 + y^2}$. Distortion coefficients are represented by OpenCV in a vector form as follows:

$$K = [k_1, k_2, p_1, p_2, k_3]$$

For the modified camera, the camera matrix is show in Fig. 4.7a. With similar values, the matrix of the unmodified camera is shown at Fig. 4.7b.

$$M_{nir} = \begin{bmatrix} 920.477 & 0 & 648.429 \\ 0 & 1027.078 & 425.516 \\ 0 & 0 & 1 \end{bmatrix} \quad (4.7a)$$

$$M_{vis} = \begin{bmatrix} 890.466 & 0 & 654.432 \\ 0 & 1001.004 & 430.778 \\ 0 & 0 & 1 \end{bmatrix} \quad (4.7b)$$

The distortion vector was slightly different in both cameras. Equation (4.8a) shows distortion coefficients for the modified cameras and (4.8b) shows the values for the

unmodified camera.

$$K_{nir} = \begin{bmatrix} -0.433 & 0.185 & -0.019 & 0.009 & 0 \end{bmatrix} \quad (4.8a)$$

$$K_{vis} = \begin{bmatrix} -0.401 & 0.165 & -0.004 & -0.004 & 0 \end{bmatrix} \quad (4.8b)$$

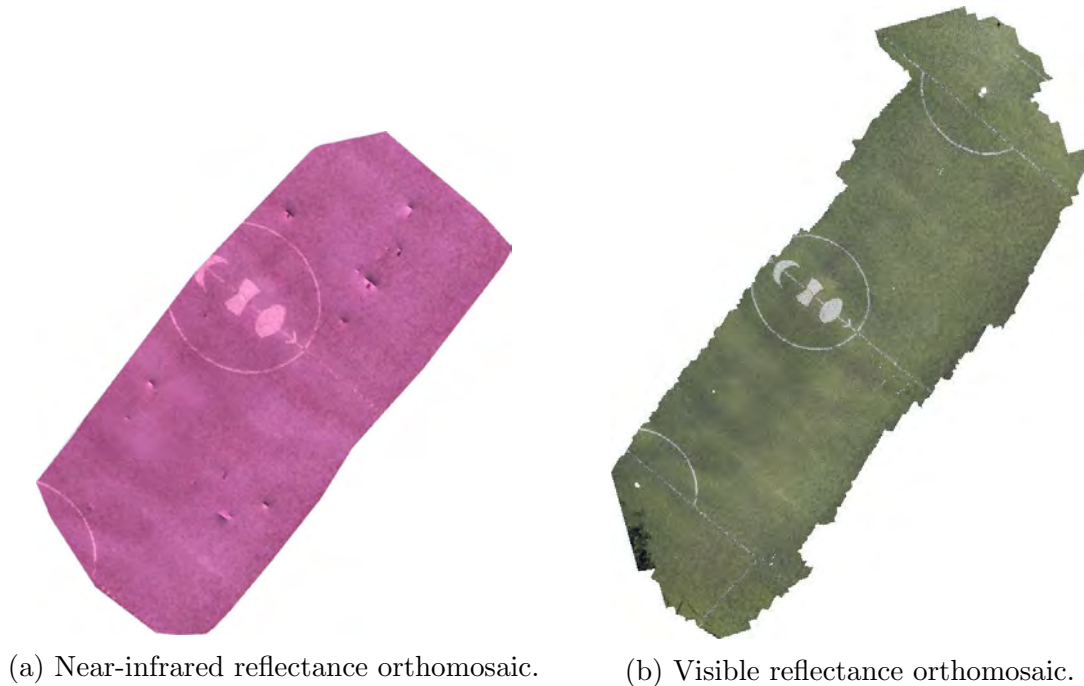
4.3.2 Image Georeferencing

As a second task, once the set of images of both cameras were collected and corrected, they were georeferenced with the Mission Planner georeferencing tool. This process is applied to the images and is also done off-line once the flight has ended. As captured images during the flight are just frames taken from the video output, they do not contain a timestamp needed to georeference them. To overcome this, a text file was filled with the exact time when an image was taken during the flight. This subtask was made by the same script that detected the trigger signal from the flight controller inside the Raspberry Pi. Naturally, the on-board computer lacks of an internal Real Time Clock (RTC), so we added an external one. With these addition, the real time could be stored. Once the file with time information was generated, a new python script was created to insert the timestamp into the correct exif tag to the images.

The timestamp insertion is the third process applied to the images just after the distortion removal. Once the timestamp was added to all the images, the georeferencing process could be started. If images matched correctly to the related *CAM* messages, then the process is done satisfactorily. At the end of the georeferencing process, a folder containing the geotagged near-infrared reflectance images and other one with the geotagged visible reflectance images were created. These sets of images are now ready to be merged into their respective orthomosaics.

4.3.3 Orthomosaic

The previously obtained sets of georeferenced images were summed individually to ODM as two separate projects. The projects were selected to be fast orthomosaics, settings some parameters to default. At the end of the process, two orthomosaics obtained from both sets of images are shown in Fig. 4.9.



(a) Near-infrared reflectance orthomosaic. (b) Visible reflectance orthomosaic.

Figure 4.9: Multispectral orthomosaics.

This process was made in a computer with Intel Core i5 at 3.2 GHz and 4 GB RAM memory. The orthomosaic generation took approximately 2 hours per orthomosaic. Around 5 tries were done before obtaining the best reconstruction. Also, the parameters were changed along this process trying to obtain a good result.

4.3.4 NDVI computation

To obtain a final NDVI orthomosaic, the resulting orthomosaics from Fig. 4.9 were used. These images are not the same size nor scale. Despite this conditions, Fiji could compute the NDVI over the common area in both orthomosaics. The obtained

image is shown at Fig. 4.10a. According to the color map in Fig. 4.10b, shades

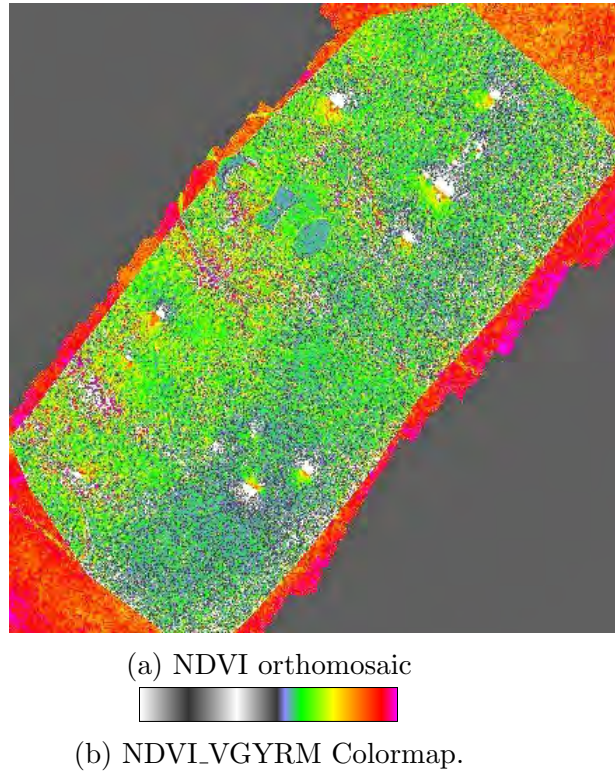


Figure 4.10: NDVI of a soccer field computed by Fiji.

of gray should be related to non-vegetative surface; green and yellow should indicate healthy vegetation; red areas should correspond to very healthy vegetation or shadows if encountered. In Fig. 4.10a the large red area was computed with that value due to the lack of data from the near-infrared orthomosaic. Green areas can be seen indicating somehow healthy vegetation but considering that the area does not contain vegetation but synthetic grass, NDVI can not be used to evaluate that area.

4.4 Additional experiments

Following part of the methodology used previously to obtain the NDVI of the soccer field with artificial grass, the computation of the NDVI was obtained from aerial imagery of a park with real vegetation. The quad-rotor equipped with the cameras was placed over a small area of a park at approximately 7 meters in *LOITER* mode. Images were

taken manually manipulating a switch in the radio control and moving the quad-rotor around that area as previously done in the camera testing section. According to Mission Planner, 20 trigger points were recorded and located as in Fig. 4.11 as green marks. It can also be seen a purple line showing the path traveled by the drone. As the quad-rotor was deployed in *STABILIZE* mode, far from the shot area, part of the purple line does not contain trigger points because vehicle was moving to the selected area.

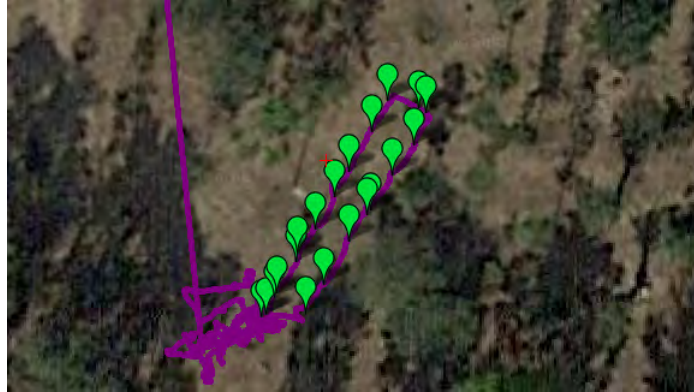


Figure 4.11: Manual trigger points on a park.

After collecting the aerial imagery, distortion was removed and timestamp was added. Then, images were georeferenced and uploaded to ODM to obtain the visible and near-infrared orthomosaics. Fig. 4.12 shows both orthomosaics.

Once the two orthomosaics were obtained, PNG format of these images were downloaded and converted into JPG images. Then, these images were used to compute NDVI with Fiji. Resultant NDVI image is shown in Fig. 4.13. According to the color map in Fig. 4.13b, red hues are related to very healthy vegetation. Comparing this image with both orthomosaics in Fig. 4.12, the red spots are generated due to the shadows of trees giving zero information about vegetation. There are also yellow and green areas that may contain healthy grass and canopy of surrounded trees. Gray hues indicates unhealthy vegetation. It is interesting to see that in Fig. 4.12a some trees appear to be dry but, in Fig. 4.12b these trees reflect near-infrared radiation which means that they are actually healthy. This can be verified in Fig. 4.13a showing trees with high NDVI values (green and yellow).

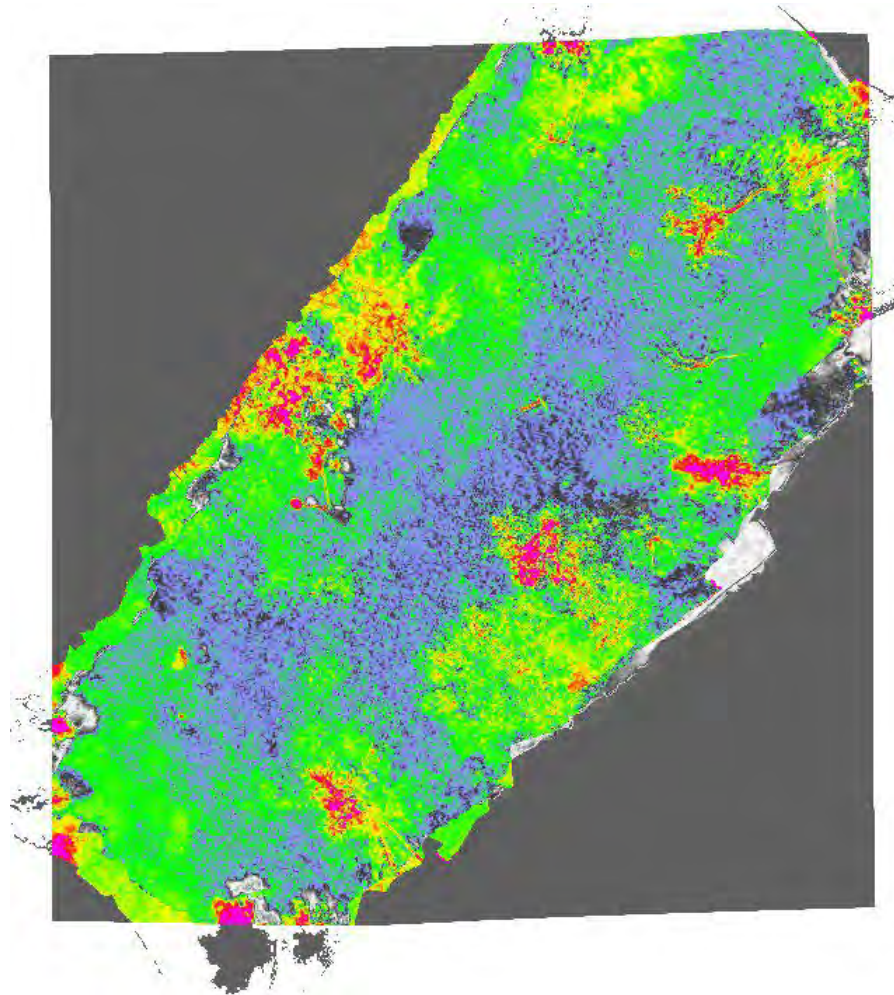


(a) Visible reflectance orthomosaic

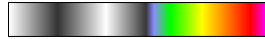


(b) Near-infrared reflectance orthomosaic.

Figure 4.12: Orthomosaics of a park.



(a) NDVI orthomosaic



(b) NDVI.VGYRM Colormap.

Figure 4.13: NDVI of a small area of a park computed by Fiji.

CHAPTER 5

Conclusions

A complete imaging system has been developed to obtain the NDVI using low-cost devices including a camera rig. One of the cameras has been modified to collect near-infrared reflectance images while the other remains unmodified to collect images of the visible spectrum. From the set of images of both cameras, individual orthomosaics are assembled to compute NDVI into a final orthomosaic. The image acquisition task worked satisfactorily during the flights. Although the image post-processing is constituted by several steps, it results in an easy-to-implement, faster, low-cost and reliable system compared to the existing options in the market.

Orthomosaics were first assembled with images containing distortion. This generated a noticeable distortion in the orthomosaic. So, eliminating the distortion increased the quality of the image. It also was noticed that ODM had some difficulty trying to merge images without texture or feature points. Customizing certain parameter in ODM solved this problem. The computation of the NDVI was done without problem using Fiji. The near-infrared and visible reflectance orthomosaics in JPG format were matched to apply the NDVI algorithm. The limitation of using JPG images is that

the resolution of the obtained NDVI image is lower compared to the original TIFF format generated by ODM. NDVI was computed in two orthomosaics obtained from different aerial imagery as shown in Fig. 4.10 and Fig. 4.13. Both reconstructions were done with success. NDVI obtained from the soccer field is not reliable due to the composition of the synthetic grass, while NDVI obtained from the park can be used to identify vegetation according to their health status.

It is important to mention that multispectral commercial cameras prices are up to \$5,000 USD, while the price of our image acquisition system is approximately \$250 USD. Considering the high cost of the commercial systems, developing low-cost versions of these systems is an issue of interest. The methodology used in this work can be reproduced with the use of any other type of camera, since the method proposed here does not involve significant modifications on the chosen devices.

In future works, it is expected to use a fixed-wing vehicle instead of a quad-rotor. Fixed-wing vehicles have a simpler structure as compared to rotary-wing UAVs, also they are capable to fly longer distances at higher speeds. They also have the advantage of longer endurance at higher speeds, thus enabling larger area coverage per flight. Finally, they can carry greater payloads for longer distances with lower power [3]. These advantages will help us to cover larger areas like crop fields in a single flight. The use of a gimbal is also planned to be implemented in the project. This could be useful to improve the quality of the captured images. Related to the camera system, the camera modification using blue filter proposed in [22] could be implemented in the imaging system to compare results with the ones obtained using the method described in this document. It is also planned to obtain aerial imagery and compute the NDVI using the RedEdge-M multispectral camera and compare that results with results already obtained with our imaging system. As an additional feature, another camera could be added to capture red edge radiation and compute the Normalized Difference Red Edge (NDRE) or the chlorophyll map as in [65].

Bibliography

- [1] A. Tariq, S. M. Osama, and A. Gillani, “Development of a low cost and light weight uav for photogrammetry and precision land mapping using aerial imagery,” in *2016 International Conference on Frontiers of Information Technology (FIT)*, Dec 2016, pp. 360–364.
- [2] H. Saari, I. Pellikka, L. Pesonen, S. Tuominen, J. Heikkil, C. Holmlund, J. Mkyinen, K. Ojala, and T. Antila, “Unmanned aerial vehicle (uav) operated spectral camera system for forest and agriculture applications,” vol. 8174, 10 2011.
- [3] J. Senthilnath, M. Kandukuri, A. Dokania, and K. Ramesh, “Application of uav imaging platform for vegetation analysis based on spectral-spatial methods,” *Computers and Electronics in Agriculture*, vol. 140, no. Supplement C, pp. 8 – 24, 2017.
- [4] V. E. R., R. Albert, A. C. A., P. N. A., S.-M. A. P., S. Srikanth, and L. A. S., “Ecohydrology with unmanned aerial vehicles,” *Ecosphere*, vol. 5, no. 10, p. art130.
- [5] L. Suárez, V. González-Dugo, and E. Fereres, “Remote sensing of vegetation from uav platforms using lightweight multispectral and thermal imaging sensors,” 2009.

- [6] F. Sabatino, “Quadrotor control: modeling, nonlinear control design, and simulation,” Master’s thesis, KTH, School of Electrical Engineering (EES), Sweden, 2015.
- [7] “Standard grade bitesize biology - making food : Revision, page 3.” [Online]. Available: http://www.bbc.co.uk/bitesize/standard/biology/world_of_plants/making_food/revision/3/
- [8] Sequoia brochure and white paper. [Online]. Available: <https://support.micasense.com/hc/en-us/articles/216631688-Sequoia-Brochure-and-White-Paper>
- [9] Vegetation and EMR. Vegetation spectral reflectance curves. [Online]. Available: http://gsp.humboldt.edu/OLM/Courses/GSP_216_Online/lesson2-1/vegetation.html
- [10] B. Siciliano and O. Khatib, *Springer Handbook of Robotics*. Secaucus, NJ, USA: Springer-Verlag New York, Inc., 2007.
- [11] MicaSense. Rededge-m. [Online]. Available: <https://www.micasense.com/rededge-m/>
- [12] Sentera. The sentera quad sensor. [Online]. Available: <https://sentera.com/product/sentera-quad-sensor/>
- [13] Tetracam. Adc lite. [Online]. Available: http://www.tetracam.com/Products-ADC_Lite.htm
- [14] M. Teke, H. S. Deveci, O. Halilolu, S. Z. Grbz, and U. Sakarya, “A short survey of hyperspectral remote sensing applications in agriculture,” in *2013 6th International Conference on Recent Advances in Space Technologies (RAST)*, June 2013, pp. 171–176.
- [15] K. Uto, H. Seki, G. Saito, and Y. Kosugi, “Development of lightweight hyperspectral imaging system for uav observation,” in *2014 6th Workshop on Hyperspectral*

- Image and Signal Processing: Evolution in Remote Sensing (WHISPERS)*, June 2014, pp. 1–4.
- [16] E. Bokolonga, M. Hauhana, N. Rollings, D. Aitchison, M. H. Assaf, S. R. Das, S. N. Biswas, V. Groza, and E. M. Petriu, “A compact multispectral image capture unit for deployment on drones,” in *2016 IEEE International Instrumentation and Measurement Technology Conference Proceedings*, May 2016, pp. 1–5.
- [17] J. A. Paredes, J. Gonzalez, C. Saito, and A. Flores, “Multispectral imaging system with uav integration capabilities for crop analysis,” in *2017 First IEEE International Symposium of Geoscience and Remote Sensing (GRSS-CHILE)*, June 2017, pp. 1–4.
- [18] T. Zhao, B. Stark, Y. Chen, A. L. Ray, and D. Doll, “A detailed field study of direct correlations between ground truth crop water stress and normalized difference vegetation index (ndvi) from small unmanned aerial system (suas),” in *2015 International Conference on Unmanned Aircraft Systems (ICUAS)*, June 2015, pp. 520–525.
- [19] Q. Xie, W. Huang, D. Liang, P. Chen, C. Wu, G. Yang, J. Zhang, L. Huang, and D. Zhang, “Leaf area index estimation using vegetation indices derived from airborne hyperspectral images in winter wheat,” *IEEE Journal of Selected Topics in Applied Earth Observations and Remote Sensing*, vol. 7, no. 8, pp. 3586–3594, Aug 2014.
- [20] E. R. Hunt, C. S. T. Daughtry, S. B. Mirsky, and W. D. Hively, “Remote sensing with unmanned aircraft systems for precision agriculture applications,” in *2013 Second International Conference on Agro-Geoinformatics (Agro-Geoinformatics)*, Aug 2013, pp. 131–134.
- [21] S. Delalieux, D. Raymaekers, K. Nackaerts, E. Honkavaara, J. Soukkamki, and J. V. D. Borne, “High spatial and spectral remote sensing for detailed mapping

- of potato plant parameters,” in *2014 6th Workshop on Hyperspectral Image and Signal Processing: Evolution in Remote Sensing (WHISPERS)*, June 2014, pp. 1–4.
- [22] J. Zhou, M. J. Pavek, S. C. Shelton, Z. J. Holden, and S. Sankaran, “Aerial multispectral imaging for crop hail damage assessment in potato,” *Computers and Electronics in Agriculture*, vol. 127, no. Supplement C, pp. 406 – 412, 2016.
- [23] S. Sankaran, L. R. Khot, J. M. Maja, and R. Ehsani, “Comparison of two multi-band cameras for use on small uavs in agriculture,” in *2013 5th Workshop on Hyperspectral Image and Signal Processing: Evolution in Remote Sensing (WHISPERS)*, June 2013, pp. 1–4.
- [24] A. Mancini, E. Frontoni, and P. Zingaretti, “A multi/hyper-spectral imaging system for land use/land cover using unmanned aerial systems,” in *2016 International Conference on Unmanned Aircraft Systems (ICUAS)*, June 2016, pp. 1148–1155.
- [25] V. M. Bure and O. A. Mitrofanova, “Analysis of color characteristics of plants using aerial photography,” in *2017 Constructive Nonsmooth Analysis and Related Topics (dedicated to the memory of V.F. Demyanov) (CNSA)*, May 2017, pp. 1–2.
- [26] T. Duan, S. Chapman, Y. Guo, and B. Zheng, “Dynamic monitoring of ndvi in wheat agronomy and breeding trials using an unmanned aerial vehicle,” *Field Crops Research*, vol. 210, no. Supplement C, pp. 71 – 80, 2017.
- [27] J. Natividade, J. Prado, and L. Marques, “Low-cost multi-spectral vegetation classification using an unmanned aerial vehicle,” in *2017 IEEE International Conference on Autonomous Robot Systems and Competitions (ICARSC)*, April 2017, pp. 336–342.
- [28] B. Jos, M. Nicols, C. Danilo, and A. Eduardo, “Multispectral ndvi aerial image system for vegetation analysis by using a consumer camera,” in *2014 IEEE Inter-*

- national Autumn Meeting on Power, Electronics and Computing (ROPEC)*, Nov 2014, pp. 1–6.
- [29] J. Navia, I. Mondragon, D. Patino, and J. Colorado, “Multispectral mapping in agriculture: Terrain mosaic using an autonomous quadcopter uav,” in *2016 International Conference on Unmanned Aircraft Systems (ICUAS)*, June 2016, pp. 1351–1358.
- [30] T. Arnold, M. D. Biasio, A. Fritz, and R. Leitner, “Uav-based measurement of vegetation indices for environmental monitoring,” in *2013 Seventh International Conference on Sensing Technology (ICST)*, Dec 2013, pp. 704–707.
- [31] P. Katsigiannis, L. Misopolinos, V. Liakopoulos, T. K. Alexandridis, and G. Zalidis, “An autonomous multi-sensor uav system for reduced-input precision agriculture applications,” in *2016 24th Mediterranean Conference on Control and Automation (MED)*, June 2016, pp. 60–64.
- [32] J. Suomalainen, N. Anders, S. Iqbal, J. Franke, P. Wenting, H. Bartholomeus, R. Becker, and L. Kooistra, “A light-weight hyperspectral mapping system for unmanned aerial vehicles; the first results,” in *2013 5th Workshop on Hyperspectral Image and Signal Processing: Evolution in Remote Sensing (WHISPERS)*, June 2013, pp. 1–4.
- [33] J. Primicerio, S. F. Di Gennaro, E. Fiorillo, L. Genesio, E. Lugato, A. Matese, and F. P. Vaccari, “A flexible unmanned aerial vehicle for precision agriculture,” *Precision Agriculture*, vol. 13, no. 4, pp. 517–523, Aug 2012.
- [34] E. Honkavaara, T. Hakala, L. Markelin, A. Jaakkola, H. Saari, H. Ojanen, I. Plnen, S. Tuominen, R. Nsi, T. Rosnell, and N. Viljanen, “Autonomous hyperspectral uas photogrammetry for environmental monitoring applications,” vol. XL-1, pp. 155–159, 11 2014.

- [35] A. Segales, R. Gregor, J. Rodas, D. Gregor, and S. Toledo, “Implementation of a low cost uav for photogrammetry measurement applications,” in *2016 International Conference on Unmanned Aircraft Systems (ICUAS)*, June 2016, pp. 926–932.
- [36] M. A. Boon, R. Greenfield, and S. Tesfamichael, “Wetland assessment using unmanned aerial vehicle (uav) photogrammetry,” vol. XLI-B1, pp. 781–788, 06 2016.
- [37] E. F. Berra, R. Gaulton, and S. Barr, “Commercial off-the-shelf digital cameras on unmanned aerial vehicles for multitemporal monitoring of vegetation reflectance and ndvi,” *IEEE Transactions on Geoscience and Remote Sensing*, vol. 55, no. 9, pp. 4878–4886, Sept 2017.
- [38] “Estimating chlorophyll with thermal and broadband multispectral high resolution imagery from an unmanned aerial system using relevance vector machines for precision agriculture,” *International Journal of Applied Earth Observation and Geoinformation*, vol. 43, no. Supplement C, pp. 32 – 42, 2015, special Issue on.
- [39] A. M. Jensen, M. Baumann, and Y. Chen, “Low-cost multispectral aerial imaging using autonomous runway-free small flying wing vehicles,” in *IGARSS 2008 - 2008 IEEE International Geoscience and Remote Sensing Symposium*, vol. 5, July 2008, pp. V – 506–V – 509.
- [40] ClaytonBarrows and D. M.Bulanon, “Development of a low-cost multispectral camera for aerial crop monitoring,” *Journal of Unmanned Vehicle Systems*, vol. 5, no. 4, pp. 192–200, 2017.
- [41] D. A. Flores, C. Saito, J. A. Paredes, and F. Trujillano, “Multispectral imaging of crops in the peruvian highlands through a fixed-wing uav system,” in *2017 IEEE International Conference on Mechatronics (ICM)*, Feb 2017, pp. 399–403.
- [42] —, “Aerial photography for 3d reconstruction in the peruvian highlands through a fixed-wing uav system,” in *2017 IEEE International Conference on Mechatronics (ICM)*, Feb 2017, pp. 388–392.

- [43] J. Goncalves and R. Henriques, “Uav photogrammetry for topographic monitoring of coastal areas,” *ISPRS Journal of Photogrammetry and Remote Sensing*, vol. 104, pp. 101 – 111, 2015.
- [44] A. Ahmad, K. N. Tahar, W. S. Udin, K. A. Hashim, N. Darwin, M. Hafis, M. Room, N. F. A. Hamid, N. A. M. Azhar, and S. M. Azmi, “Digital aerial imagery of unmanned aerial vehicle for various applications,” in *2013 IEEE International Conference on Control System, Computing and Engineering*, Nov 2013, pp. 535–540.
- [45] A. L. Chan, S. L. Tan, and C. L. Kwek, “Sensor data fusion for attitude stabilization in a low cost quadrotor system,” in *2011 IEEE 15th International Symposium on Consumer Electronics (ISCE)*, June 2011, pp. 34–39.
- [46] R. W. Beard and T. W. McLain, *Small Unmanned Aircraft: Theory and Practice*. Princeton, NJ, USA: Princeton University Press, 2012.
- [47] T. S Alderete, “Simulator aero model implementation,” 05 2018.
- [48] S. G. Systems. Rededge-m. [Online]. Available: <https://smartgrow.systems/plant-light-dli-calculator/>
- [49] Y. Sun, X.-F. Wang, G. Chen, C.-H. Zhan, O. Kitao, H. Tamiaki, and S. ichi Sasaki, “Near-infrared absorption carboxylated chlorophyll-a derivatives for bio-compatible dye-sensitized hydrogen evolution,” *International Journal of Hydrogen Energy*, vol. 42, no. 24, pp. 15 731 – 15 738, 2017.
- [50] D. Pavlovic, B. Nikolic, S. Djurovic, H. Waisi, A. Andjelkovic, and D. Marisavljevic, “Chlorophyll as a measure of plant health: Agroecological aspects,” vol. 29, pp. 21–34, 03 2014.
- [51] M. Khayatnezhad, “The effect of drought stress on leaf chlorophyll content and stress resistance in maize cultivars (zea mays),” vol. 6, 03 2012.

- [52] “Chapter 10 - canopy biochemical characteristics,” in *Advanced Remote Sensing*, S. Liang, X. Li, and J. Wang, Eds. Boston: Academic Press, 2012, pp. 301 – 346.
- [53] G. A. Carter and A. K. Knapp, “Leaf optical properties in higher plants: linking spectral characteristics to stress and chlorophyll concentration,” *American Journal of Botany*, vol. 88, no. 4, pp. 677–684.
- [54] J. Verdebout, S. Jacquemoud, and G. Schmuck, *Optical Properties of Leaves: Modelling and Experimental Studies*. Dordrecht: Springer Netherlands, 1994, pp. 169–191.
- [55] R. Kumar and L. Silva, “Reflectance model of a plant leaf,” 1973.
- [56] C. Daughtry, C. Walthall, M. Kim, E. de Colstoun, and J. McMurtrey, “Estimating corn leaf chlorophyll concentration from leaf and canopy reflectance,” *Remote Sensing of Environment*, vol. 74, no. 2, pp. 229 – 239, 2000.
- [57] R. Fensholt and I. Sandholt, “Derivation of a shortwave infrared water stress index from modis near- and shortwave infrared data in a semiarid environment,” *Remote Sensing of Environment*, vol. 87, no. 1, pp. 111 – 121, 2003.
- [58] P. P. D. Autopilot, “Pixhack v3.” [Online]. Available: [https://docs.px4.io/en/flight_controller/pixhack_v3.html](https://docs.px4.io/en/flight/_controller/pixhack_v3.html)
- [59] A. D. Team. Ardupilot. [Online]. Available: <http://ardupilot.org/>
- [60] Opendronemap. [Online]. Available: <http://opendronemap.org/>
- [61] J. Schindelin and I. . F. Arganda-Carreras, “Fiji: An open-source platform for biological-image analysis,” vol. 9, pp. 676–82, 06 2012.
- [62] B. A. DeWitt and P. R. Wolf, *Elements of Photogrammetry(with Applications in GIS)*, 3rd ed. McGraw-Hill Higher Education, 2000.

- [63] “Standard grade bitesize biology - making food : Revision, page 3.” [Online]. Available: http://www.bbc.co.uk/bitesize/standard/biology/world_of_plants/making_food/revision/3/
- [64] G. Bradski and A. Kaehler, *Learning OpenCV: Computer Vision with the OpenCV Library*. United States of America: O’Reilly Media, 2008.
- [65] S. Delalieux, D. Raymaekers, K. Nackaerts, E. Honkavaara, J. Soukkamki, and J. V. D. Borne, “High spatial and spectral remote sensing for detailed mapping of potato plant parameters,” in *2014 6th Workshop on Hyperspectral Image and Signal Processing: Evolution in Remote Sensing (WHISPERS)*, June 2014, pp. 1–4.